The Astronomical Journal, 161:106 (17pp), 2021 March https://doi.org/10.3847/1538-3881/abd243

The McDonald Accelerating Stars Survey (MASS): White Dwarf Companions Accelerating the Sun-like Stars 12 Psc and HD 159062

Brendan P. Bowler[1], William D. Cochran[2], Michael Endl[3], Kyle Franson[1], Timothy D. Brandt[4], Trent J. Dupuy[5], Phillip J. MacQueen[3], Kaitlin M. Kratter[6], Dimitri Mawet[7], and Garreth Ruane[7]
[1] Department of Astronomy, The University of Texas at Austin, Austin, TX 78712, USA; bpbowler@astro.as.utexas.edu
[2] Center for Planetary Systems Habitability and McDonald Observatory, The University of Texas at Austin, Austin, TX 78712, USA
[3] McDonald Observatory and the Department of Astronomy, The University of Texas at Austin, Austin, TX 78712, USA
[4] Department of Physics, University of California, Santa Barbara, Santa Barbara, CA 93106, USA
[5] Gemini Observatory, Northern Operations Center, 670 N. A ohoku Place, Hilo, HI 96720, USA
[6] Department of Astronomy, University of Arizona, Tucson, AZ 85721, USA
[7] Department of Astronomy, California Institute of Technology, Pasadena, CA 91125, USA
Received 2020 October 30; revised 2020 December 8; accepted 2020 December 8; published 2021 February 8

Abstract

We present the discovery of a white dwarf companion to the G1 V star 12 Psc found as part of a Keck adaptive optics imaging survey of long-term accelerating stars from the McDonald Observatory Planet Search Program. Twenty years of precise radial-velocity monitoring of 12 Psc with the Tull Spectrograph at the Harlan J. Smith telescope reveals a moderate radial acceleration ($\approx$10 m s^{-1} yr^{-1}), which together with relative astrometry from Keck/NIRC2 and the astrometric acceleration between Hipparcos and Gaia DR2 yields a dynamical mass of $M_B = 0.605^{+0.021}_{-0.022} M_\odot$ for 12 Psc B, a semimajor axis of 40^{+2}_{-4} au, and an eccentricity of 0.84 ± 0.08. We also report an updated orbital fit of the white dwarf companion to the metal-poor (but barium-rich) G9 V dwarf HD 159062 based on new radial-velocity observations from the High-Resolution Spectrograph at the Hobby–Eberly Telescope and astrometry from Keck/NIRC2. A joint fit of the available relative astrometry, radial velocities, and tangential astrometric acceleration yields a dynamical mass of $M_B = 0.609^{+0.010}_{-0.011} M_\odot$ for HD 159062 B, a semimajor axis of 60^{+5}_{-7} au, and preference for circular orbits ($e < 0.42$ at 95% confidence). 12 Psc B and HD 159062 B join a small list of resolved Sirius-like benchmark white dwarfs with precise dynamical mass measurements which serve as valuable tests of white dwarf mass–radius cooling models and probes of AGB wind accretion onto their main-sequence companions.

Unified Astronomy Thesaurus concepts: White dwarf stars (1799); Direct imaging (387); Binary stars (154); Astrometric binary stars (79); Radial velocity (1332); Orbit determination (1175)

Supporting material: machine-readable tables

1. Introduction

Dynamical masses represent anchor points of stellar astronomy. Direct mass measurements are important to calibrate models of stellar and substellar evolution, especially during phases in which physical properties change significantly with time—for example throughout the pre-main-sequence, along the evolved subgiant and giant branches, and as white dwarfs, brown dwarfs, and giant planets cool and fade over time (e.g., Hillenbrand & White 2004; Konopacky et al. 2010; Bond et al. 2017a; Dupuy & Liu 2017; Parsons et al. 2017; Snellen & Brown 2018; Brandt et al. 2019; Simon et al. 2019). Masses are traditionally determined with absolute astrometry of visual binaries or radial-velocity (RV) monitoring of either eclipsing or visual binaries. Other approaches include modeling Keplerian rotation of resolved protoplanetary disks, gravitational lensing, and transit-timing variations in the case of close-in planets (see Serenelli et al. 2020 for a recent review).

It is especially challenging to measure dynamical masses of nontransiting binaries when one component is faint, as is the case of white dwarf, brown dwarf, or giant planet companions to stars. With high-contrast adaptive optics (AO) imaging, there is a pragmatic trade-off between separation and contrast: short period companions reveal their orbits on faster timescales but are more challenging to detect, whereas more distant companions are easier to image but orbit more slowly. Similarly, RV precision, stellar activity, and time baseline of the observations compete when measuring a radial acceleration induced on the star by the companion. The optimal region in which radial reflex accelerations can be measured and faint companions can be imaged with current facilities is ~5–100 au. Most of the known benchmark white dwarf, brown dwarf, and giant planet companions fall in this range of orbital distances (see, e.g., Table 2 of Bowler 2016).

One of the most successful means of identifying these faint degenerate companions (whose pressure support predominantly originates from electron degeneracy) with direct imaging has been by using radial accelerations on their host stars, which can act as dynamical beacons that betray the presence of a distant companion. Long-baseline RV surveys are especially well suited for this task, such as the California Planet Survey (Howard et al. 2010), Lick–Carnegie Exoplanet Survey (Butler et al. 2017), McDonald Observatory Planet Search (Cochran & Hatzes 1993), Lick Planet Search (Fischer et al. 2014), Anglo-Australian Planet Search (Tinney et al. 2001), and CORALIE survey for extrasolar planets (Queloz et al. 2000). With baselines spanning several decades and sample sizes of thousands of targets, these programs have facilitated the discovery and characterization of a growing list of substellar companions (HR 7672 B, Liu et al. 2002; HD 19467 B, Crepp et al. 2014; HD 4747 B, Crepp et al. 2016; HD 4113 C, Cheetham et al. 2018; Gl 758 B, Thalmann et al. 2009;

Bowler et al. 2018; HD 13724 B, Rickman et al. 2020; HD 72946 B, Maire et al. 2020; HD 19467 B, Maire et al. 2020; Gl 229 B, Nakajima et al. 1995; Brandt et al. 2020) and white dwarf companions (Gl 86 B, Els et al. 2001; Mugrauer & Neuhäuser 2005; HD 8049 B, Zurlo et al. 2013; HD 114174 B, Crepp et al. 2013; HD 11112 B, Rodigas et al. 2016; HD 169889 B, Crepp et al. 2018; HD 159062 B, Hirsch et al. 2019) with direct imaging. Only a handful of these degenerate companions have dynamically measured masses, although recent efforts to determine astrometric accelerations on their host stars using Hipparcos and Gaia are increasing these numbers (e.g., Calissendorff & Janson 2018; Brandt et al. 2019; Dupuy et al. 2019).

To find new benchmark companions and measure their dynamical masses, we launched the McDonald Accelerating Stars Survey (MASS), a high-contrast imaging program targeting stars with radial accelerations based on RV planet search programs at McDonald Observatory. The McDonald Observatory Planet Search began in 1987 at the 2.7-m Harlan J. Smith Telescope and is among the oldest RV planet surveys (Cochran & Hatzes 1993). The most recent phase of the survey using the Tull Spectrograph commenced in 1998 and continues today. In addition to discoveries of giant planets spanning orbital periods of a few days to over 10 years (e.g., Cochran et al. 1997; Hatzes et al. 2003; Robertson et al. 2012; Endl et al. 2016), many shallow long-term accelerations have been identified over the past three decades. Accelerating stars in our sample also draw from a planet search around 145 metal-poor stars using the 9.2 m Hobby–Eberly Telescope's High-Resolution Spectrograph (HRS). This program operated from 2008 to 2013 and, like the McDonald Observatory Planet Search, identified both planets and longer-term radial accelerations (Cochran & Endl 2008).

In Bowler et al. (2018) we presented an updated orbit and mass measurement of the late-T dwarf Gl 758 B as part of this program based on new imaging data and RVs from McDonald Observatory, Keck Observatory, and the Automated Planet Finder. The mass of Gl 758 B was subsequently refined in Brandt et al. (2019) by taking into account the proper-motion difference between Hipparcos and Gaia. Here we present the discovery and dynamical mass measurement of a faint white dwarf companion to the Sun-like star 12 Psc based on a long-term RV trend of its host star from the McDonald Observatory Planet Search. In addition, we present an updated orbit and mass measurement of HD 159062 B, a white dwarf companion to an accelerating G9 V star recently discovered by Hirsch et al. (2019) and independently identified in our program using RVs from HRS. These objects join only a handful of other resolved white dwarf companions with dynamical mass measurements.

This paper is organized as follows. In Section 2 we provide an overview of the properties of 12 Psc and HD 159062. Section 3 describes the RV and imaging observations of these systems from McDonald Observatory and Keck Observatory. The orbital fits and dynamical mass measurements for both companions are detailed in Section 4. Finally, we discuss the implications of the mass measurements for the evolutionary history of the system in Section 5.

2. Overview of 12 Psc and HD 159062

12 Psc (=HD 221146, HIP 115951) is a bright ($V = 6.9$ mag) G1 V dwarf (Gray et al. 2006) located at a parallactic distance of 36.2 ± 0.06 pc (Gaia Collaboration et al. 2018). Spectroscopy and isochrone fitting imply a slightly more massive, older, and more metal-rich analog to the Sun. For example, Soto & Jenkins (2018) find an age of $5.3^{+1.1}_{-1.0}$ Gyr, a mass of $1.11 \pm 0.05\ M_{\odot}$, a metallicity of $[\mathrm{Fe/H}] = 0.13 \pm 0.10$ dex, and an effective temperature of 5950 ± 50 K. This is in good agreement with other recent analysis from Tsantaki et al. (2013), Marsden et al. (2014), and Aguilera-Gómez et al. (2018). The old age is bolstered by the low activity level, with $\log R'_{\mathrm{HK}}$ values ranging from −5.06 dex to −4.86 dex (e.g., Isaacson & Fischer 2010; Murgas et al. 2013; Saikia et al. 2018). A summary of the physical, photometric, and kinematic properties of 12 Psc can be found in Table 1.

Table 1
Properties of 12 Psc

Parameter	Value	Reference
Physical Properties		
$\alpha_{2000.0}$	23:29:30.31	...
$\delta_{2000.0}$	−01:02:09.1	...
π (mas)	27.60 ± 0.05	1
Distance (pc)	36.23 ± 0.06	1
SpT	G1 V	2
Mass ($M_{\odot}$)	1.11 ± 0.05	3
Age (Gyr)	5.3 ± 1.1	3
T_{eff} (K)	5950 ± 50	3
$\log(L_{\mathrm{bol}}/L_{\odot})$	0.358 ± 0.08	4
$\log g$ (dex) [cgs]	4.34 ± 0.3	3
R ($R_{\odot}$)	1.32 ± 0.03	3
[Fe/H] (dex)	$+0.13 \pm 0.10$	3
$v \sin i$ (km s^{-1})	2.3 ± 0.2	3
$\log R'_{\mathrm{HK}}$	-5.07 ± 0.01	4
Proj. Sep. ($''$)	1.6	5
Proj. Sep. (au)	58	5
dv_r/dt (m s^{-1} yr^{-1})	10.60 ± 0.13	5
Photometry		
V (mag)	6.92 ± 0.04	6
Gaia G (mag)	6.7203 ± 0.0003	1
J (mag)	5.77 ± 0.01	7
H (mag)	5.49 ± 0.03	7
K_S (mag)	5.40 ± 0.01	7
HGCA Kinematics[a]		
$\mu_{\alpha,\mathrm{Hip}}$ (mas yr^{-1})	-11.97 ± 1.09	8
$\mu_{\alpha,\mathrm{Hip}}$ Epoch (yr)	1991.348	8
$\mu_{\delta,\mathrm{Hip}}$ (mas yr^{-1})	-28.50 ± 0.84	8
$\mu_{\delta,\mathrm{Hip}}$ Epoch (yr)	1991.277	8
$\mu_{\alpha,\mathrm{HG}}$ (mas yr^{-1})	-11.32 ± 0.03	8
$\mu_{\delta,\mathrm{HG}}$ (mas yr^{-1})	-25.66 ± 0.02	8
$\mu_{\alpha,\mathrm{Gaia}}$ (mas yr^{-1})	-10.54 ± 0.12	8
$\mu_{\alpha,\mathrm{Gaia}}$ Epoch (yr)	2015.563	8
$\mu_{\delta,\mathrm{Gaia}}$ (mas yr^{-1})	-24.24 ± 0.09	8
$\mu_{\delta,\mathrm{Hip}}$ Epoch (yr)	2015.669	8
$\Delta\mu_{\alpha,\mathrm{Gaia-HG}}$ (mas yr^{-1})	0.78 ± 0.12	8
$\Delta\mu_{\delta,\mathrm{Gaia-HG}}$ (mas yr^{-1})	1.42 ± 0.09	8
$d\mu_{\alpha\delta}/dt$ (m s^{-1} yr^{-1})	22.9 ± 1.4	8

Notes. (1) Gaia Collaboration et al. (2018); (2) Gray et al. (2006); (3) Soto & Jenkins (2018); (4) Marsden et al. (2014); (5) this work; (6) Richmond et al. (2000); (7) Cutri et al. (2003); (8) Brandt (2018).
[a] Hipparcos–Gaia Catalog of Accelerations (Brandt 2018). Proper motions in R.A. include a factor of $\cos\delta$.

HD 159062 is an old, metal-poor, main-sequence G9 V star (Gray et al. 2003) located at a distance of 21.7 pc (Gaia Collaboration et al. 2018). Hirsch et al. (2019) inferred a mass of $0.76 \pm 0.03\,M_{\odot}$ using spectroscopically derived physical properties and stellar isochrones. A wide range of ages have been determined for HD 159062 in the literature: Isaacson & Fischer (2010) and Hirsch et al. (2019) find activity-based ages of $\approx$6 Gyr and $\approx$7 Gyr using $R'_{\rm HK}$ values, while typical isochrone-based ages range from 9.2 ± 3.5 Gyr from Luck (2017) to $13.0^{+1.4}_{-2.4}$ Gyr from Brewer et al. (2016). Brewer & Carney (2006) measure a metallicity of [Fe/H] = −0.50 dex and find that HD 159062 has an 88% probability of belonging to the thick disk based on its kinematics. HD 159062 also exhibits an enhancement of α-capture elements such as [Mg/Fe], [Si/Fe], and [Ca/Fe], further supporting membership in the thick disk. The low-metallicity, enhanced [α/Fe] abundances and thick-disk kinematics point to an older age for this system. Brewer & Carney (2006) also note that HD 159062 exhibits substantially enhanced *s*-process elements and suggest this could have been caused by mass transfer from an evolved AGB companion. This scenario is supported by Fuhrmann et al. (2017), who find an anomalously high barium abundance and conclude that HD 159062 may harbor a white dwarf companion. This prediction was realized with the discovery of HD 159062 B by Hirsch et al. (2019) using a long-baseline RV trend from Keck/High Resolution Echelle Spectrometer (HIRES) and follow-up AO imaging. They determine a dynamical mass of $0.65^{+0.12}_{-0.04}\,M_{\odot}$ for HD 159062 B, which was refined by Brandt et al. (2020, submitted) to $0.617^{+0.013}_{-0.012}$ $M_{\odot}$ after adding in the astrometric acceleration induced on the host star using Hipparcos and Gaia (see Section 4.4).

3. Observations

3.1. Radial Velocities

3.1.1. Harlan J. Smith Telescope/Tull Spectrograph Radial Velocities of 12 Psc

Fifty RV measurements of 12 Psc were obtained with the Tull Coudé spectrograph (Tull et al. 1995) at McDonald Observatory's 2.7-m Harlan J. Smith telescope between 2001 and 2020. All observations used the 1.″2 slit, resulting in a resolving power of $R \equiv \lambda/\Delta\lambda \approx 60{,}000$. A temperature-stabilized gas cell containing molecular iodine vapor (I_2) is mounted in the light path before the slit entrance, enabling precise RV measurements with respect to an iodine-free template following the description in Endl et al. (2000). RVs are subsequently corrected for Earth's barycentric motion as well as the small secular acceleration for 12 Psc ($0.000582\,\mathrm{m\,s^{-1}\,yr^{-1}}$). The time of observation is corrected to the barycentric dynamical time as observed at the solar system barycenter. Observations starting in 2009 take into account the flux-weighted barycentric correction of each observation using an exposure meter. The RVs are shown in Figure 1 and are listed in Table 2.[8] The median measurement uncertainty is $5.1\,\mathrm{m\,s^{-1}}$.

12 Psc shows a constant acceleration away from the Sun with no obvious signs of curvature, indicating that a companion orbits this star with a period substantially longer than the time baseline of the observations ($P \gg 20$ yr). A linear fit to the McDonald RVs gives a radial acceleration of $dv_r/dt = 10.60 \pm 0.13\,\mathrm{m\,s^{-1}\,yr^{-1}}$.

12 Psc was also observed with the Hamilton Spectrograph at Lick Observatory as part of the Lick Planet Search (Fischer et al. 2014) between 1998 and 2012. 109 RVs were obtained with a typical precision of $4.4\,\mathrm{m\,s^{-1}}$. A linear fit to the Lick RVs gives a slope of $dv_r/dt = 9.78 \pm 0.15\,\mathrm{m\,s^{-1}\,yr^{-1}}$ (Figure 1). This is slightly shallower than the slope from the McDonald RVs (at the 4σ level), which may indicate modest change in acceleration between the mean epochs of both data sets (2004.0 for Lick and 2009.7 for McDonald).

3.1.2. Hobby–Eberly Telescope/High-resolution Spectrograph Radial Velocities of HD 159062

HD 159062 was monitored with HRS at the Hobby–Eberly Telescope (HET) between 2008 and 2014. HRS is a fiber-fed echelle spectrograph located in the basement of the HET (Tull 1998), and is passively (rather than actively) thermally and mechanically stabilized. A temperature controlled I_2 cell is mounted in front of the entrance slit and is used as a reference for RV measurements. Sixty-four high signal-to-noise ratio (S/N) spectra were acquired with the HET's flexible queue scheduling system (Shetrone et al. 2007) with a resolving power of $R \approx 60{,}000$ between 4110 Å and 7875 Å. Relative RVs are measured in spectral chunks following the procedure described in Cochran et al. (2003) and Cochran et al. (2004). The median RV uncertainty is $3.4\,\mathrm{m\,s^{-1}}$.

The HRS RVs of HD 159062 are shown in Figure 2. We find an acceleration of $dv_r/dt = -14.1 \pm 0.3\,\mathrm{m\,s^{-1}\,yr^{-1}}$, which is similar to the slope of $-13.30 \pm 0.12\,\mathrm{m\,s^{-1}\,yr^{-1}}$ from Hirsch et al. (2019) based on 45 Keck/HIRES RVs spanning 2003 to 2019. A slight curvature is seen in the HIRES data; this changing acceleration is not evident in our HRS data, most likely owing to the shorter time baseline compared to the HIRES data. A list of our HRS RVs can be found in Table 3.

3.2. Keck/NIRC2 Adaptive Optics Imaging

We imaged 12 Psc and HD 159062 with the NIRC2 infrared camera in its narrow configuration ($9.971\,\mathrm{mas\,pix^{-1}}$ plate scale; Service et al. 2016) using natural guide star AO at Keck Observatory (Wizinowich et al. 2000; Wizinowich 2013). 12 Psc was initially targeted as part of this program on 2017 October 10 UT with subsequent observations on 2018 December 24 UT and 2019 July 07 UT. HD 159062 was observed on 2017 October 10 UT and 2019 July 07 UT. For each observation, the star was centered behind the partly transparent 600 mas diameter coronagraph to avoid saturation when reading out the full $10.″2 \times 10.″2$ array. Most sequences consist of five coronagraphic ("reconnaissance") images with the *H*- or K_S-band filters to search for readily identifiable long-period stellar or substellar companions.

12 Psc B and HD 159062 B were immediately evident in the raw frames, although it was not clear whether they were faint white dwarfs, brown dwarfs, or background stars at the time of discovery. We also acquired deeper sequences in pupil-tracking mode (or angular differential imaging; Marois et al. 2006) in 2019 July to search for additional companions at smaller separations. These observations consisted of forty 30 s frames; for 12 Psc the total field rotation was 11.°6 and for HD 159062 the total rotation was 16.°4. On the 2017 October and 2019 July

[8] Note that the measured RVs are determined with respect to a dense set of iodine absorption lines rather than an absolute reference, such as a stable RV standard. The zero-point is therefore arbitrary.

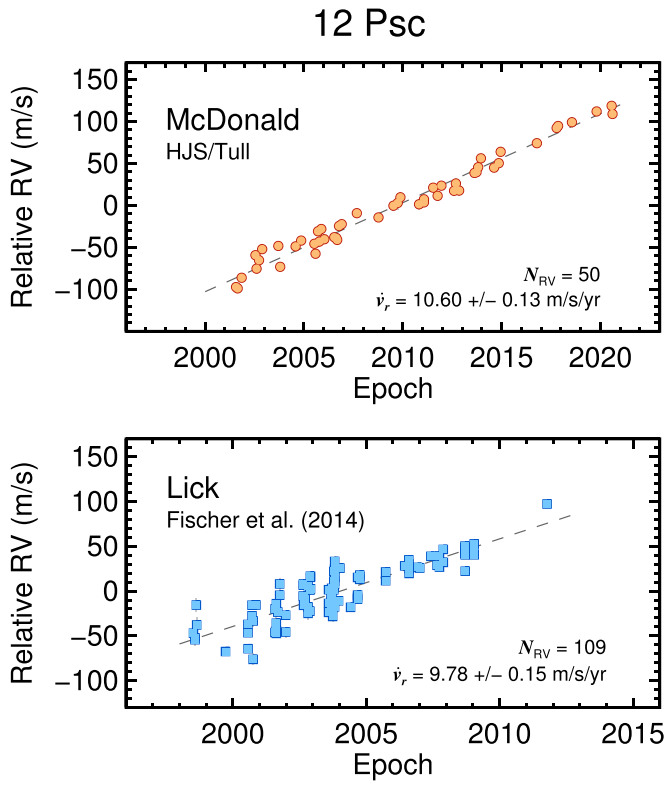

Figure 1. Radial velocities of 12 Psc from McDonald Observatory (top) and Lick Observatory (bottom; Fischer et al. 2014) spanning a total baseline of over 20 years (1998–2020). A strong radial acceleration is evident in both data sets. A linear fit gives a slope of 10.60 ± 0.13 m s^{-1} yr^{-1} for the Tull RVs and 9.78 ± 0.15 m s^{-1} yr^{-1} for the Lick RVs.

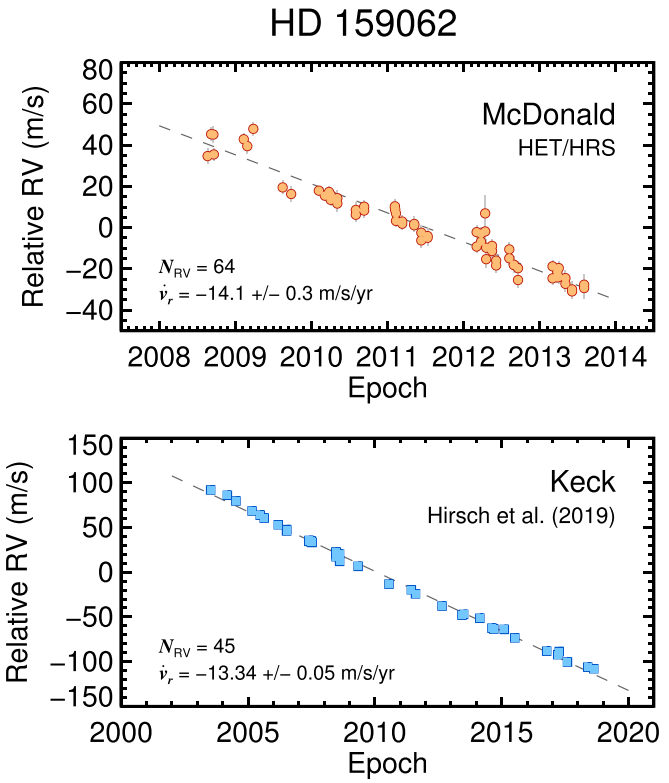

Figure 2. Radial velocities of HD 159062 from HET/HRS (top) and Keck/HIRES (bottom; Hirsch et al. 2019). A linear fit to the HRS and HIRES data sets give accelerations of -14.1 ± 0.3 m s^{-1} yr^{-1} and -13.34 ± 0.05 m s^{-1} yr^{-1}, respectively.

Table 2
Tull Spectrograph Relative Radial Velocities of 12 Psc

Date (BJD)	RV (m s^{-1})	σ_{RV} (m s^{-1})
2452115.95277	−97.23	3.69
2452145.89854	−98.83	4.20
2452219.66771	−86.14	5.03
2452473.90774	−59.28	4.44
2452494.83891	−75.32	6.33
2452540.79863	−65.29	5.13
2452598.71506	−52.06	4.50
2452896.84418	−48.27	5.57
2452931.83102	−73.12	4.71
	…	

Note. Table 2 is published in its entirety in the machine-readable format. A portion is shown here for guidance regarding its form and content.

(This table is available in its entirety in machine-readable form.)

Table 3
HRS Relative Radial Velocities of HD 159062

Date (BJD)	RV (m s^{-1})	σ_{RV} (m s^{-1})
2454698.72895	34.67	3.77
2454715.68103	45.29	3.29
2454726.62674	45.12	3.95
2454728.63730	35.47	3.13
2454873.01630	42.84	2.98
2454889.98057	39.49	3.39
2454918.88920	47.88	3.21
2455059.74200	19.49	3.33
2455100.63545	16.31	3.76
2455261.94792	15.50	2.62
	…	

Note. Table 3 is published in its entirety in the machine-readable format. A portion is shown here for guidance regarding its form and content.

(This table is available in its entirety in machine-readable form.)

nights we also acquired short unsaturated images immediately following the coronagraphic images to photometrically calibrate the deeper frames. A summary of our observations can be found in Table 4.

We searched the Keck Observatory Archive and found that 12 Psc was also imaged on two separate occasions with NIRC2 in 2004 September and 2005 July (PI: M. Liu) in J and K_p bands, respectively. Both sequences consist of coronagraphic images similar to our observations with the host star centered behind the occulting spot. 12 Psc B is visible in both frames, offering a 15-year astrometric baseline to test for common proper motion and measure orbital motion.

Basic data reduction was carried out in the same fashion for all images, which consisted of flat-fielding using dome flats, correction for bad pixels and cosmic rays, and correction for geometric field distortion using the solutions derived by Yelda et al. (2010) for observations taken before 2015 April (when the AO system was realigned) and Service et al. (2016) for images taken after that date. For both distortion solutions, the direction of celestial north was calibrated by tying NIRC2 observations of globular clusters to distortion-corrected stellar

Table 4
Keck/NIRC2 Adaptive Optics Imaging

UT Date (Y M D)	Epoch (UT)	$N \times$ Coadds$\times t_{exp}$ (s)	Filter	Sep. (″)	P.A. (°)	Contrast (Δ mag)	PSF Sub.[a]
			12 Psc B				
2004 Sep 08	2004.688	$7 \times 1 \times 30$	J+cor600	1.723 ± 0.005	28.63 ± 0.10	⋯	⋯
2005 Jul 15	2005.536	$12 \times 2 \times 15$	K_p+cor600	1.720 ± 0.005	28.5 ± 0.2	⋯	1
2017 Oct 10	2017.773	$5 \times 6 \times 5$	H+cor600	1.623 ± 0.005	25.10 ± 0.14	10.38 ± 0.16	2, 3, 4
2018 Dec 24	2018.978	$5 \times 6 \times 5$	H+cor600	1.600 ± 0.005	24.33 ± 0.12	⋯	2, 3, 4
2018 Dec 24	2018.978	$5 \times 6 \times 5$	K_S+cor600	1.604 ± 0.005	24.26 ± 0.13	⋯	2, 3, 4
2019 Jul 07	2019.514	$40 \times 3 \times 10$	K_S+cor600	1.592 ± 0.005	24.4 ± 0.2	10.53 ± 0.01	2
			HD 159062 B				
2017 Oct 10	2017.773	$5 \times 5 \times 3$	H+cor600	2.663 ± 0.005	301.34 ± 0.11	⋯	⋯
2019 Jul 07	2019.513	$40 \times 10 \times 3$	H+cor600	2.702 ± 0.005	301.9 ± 0.4	⋯	2, 3

Note.
[a] PSF subtraction method: (1) scaled median subtraction; (2) conservative LOCI with parameters $W = 5$, $N_A = 300$, $g = 1$, $N_\delta = 1.5$, and $dr = 2$; (3) 100 additional images used from the PSF reference library; (4) companion masked during PSF subtraction. See Bowler et al. (2015a) and Bowler et al. (2015b) for additional details.

positions obtained with the Hubble Space Telescope. The resulting precision in the north orientation is ≈0.001–0.°002—much less than the typical measurement uncertainties for AO-based relative astrometry.

Images in each coronagraph sequence are aligned by fitting a 2D elliptical Gaussian to the host star, which is visible behind the partly transparent mask, then shifting each image with subpixel precision to a common position. We attempted several approaches to point-spread function (PSF) subtraction for each sequence in order to increase the S/N of the companion: subtraction of a scaled median image of the sequence, a conservative implementation of the Locally Optimized Combination of Images (LOCI; Lafrenière et al. 2007), an aggressive form of LOCI with a more restrictive angular tolerance parameter, LOCI using 100 images selected in an automated fashion from a NIRC2 reference PSF library comprising $>2 \times 10^3$ registered coronagraph frames, and optional masking of the companion during PSF subtraction. Details of these methods and the NIRC2 PSF library are described in Bowler et al. (2015a) and Bowler et al. (2015b). We attempted PSF subtraction for the 2004 observations of 12 Psc and the 2017 observations of HD 159062 but strong systematics were present in the residuals. The final processed images we adopt for this study are shown in Figures 3 and 4. Table 4 lists the observations and the adopted PSF subtraction method.

In general, astrometry and relative photometry of point sources measured directly from processed (PSF-subtracted) images can be biased as a result of self-subtraction and nonuniform field-of-view rotation. These effects can be especially severe for longer angular differential imaging (ADI) data sets (e.g., Marois et al. 2010). When possible we use the negative PSF injection approach described in Bowler et al. (2018) to mitigate these biases. This entails adding a PSF with a negative amplitude close to the position of the point source in the raw images, running PSF subtraction at that position, and measuring the rms of the residuals in a circular aperture. This process is then iteratively repeated by varying the astrometry (ρ and θ) at the subpixel level and the flux ratio (simply the amplitude of the negative PSF) using the `amoeba` algorithm (Nelder & Mead 1965; Press et al. 2007) until the resulting rms is minimized. This method requires a PSF model; if unsaturated frames of the host star are taken close in time to the ADI sequence (to avoid changes in atmospheric conditions and AO correction), this approach can be used to reliably measure the contrast between the host star and the faint point source. When no unsaturated frames are available, any PSF can be used to measure astrometry (but not relative photometry).

We use this negative PSF injection approach to measure astrometry for the ADI data sets of 12 Psc and HD 159062 taken in 2019 July. In both cases, images of 12 Psc without the coronagraph mask are used as the PSF model since unsaturated images of HD 159062 were not taken on 2019 July. We also use this approach to measure relative photometry and astrometry of 12 Psc for the 2017 October data set because unsaturated frames were acquired. Uncertainties in the relative photometry are estimated using the mean of the final 10 iterations of the `amoeba` downhill simplex algorithm as the negative PSF separation, position angle, and amplitude settle in at values that minimize the rms at the position of the companion. For all other observations, relative astrometry is directly computed from the unprocessed images. Total astrometric uncertainties are derived following Bowler et al. (2018) and incorporate random measurement uncertainties, systematic errors from the distortion solution, uncertainty in the plate scale and north angle, and shear (PSF blurring) caused by field rotation within an exposure. Because the coronagraph mask may introduce an additional uncalibrated source of systematic uncertainty (e.g., Konopacky et al. 2016; Bowler et al. 2018), we conservatively adopt 5 mas and 0.1° as the floor for separation and position angle uncertainties, respectively. Final values for 12 Psc B and HD 159062 B can be found in Table 4.[9]

4. Results

4.1. Common Proper Motion

Figure 5 shows the expected relative motion of a stationary background source due to the proper and projected parallactic motion of 12 Psc. 12 Psc B is clearly comoving and exhibits significant orbital motion in separation and position angle. A

[9] Note that position angles in this work correspond to the angle from celestial north through east at the epoch of observation, not for J2000.

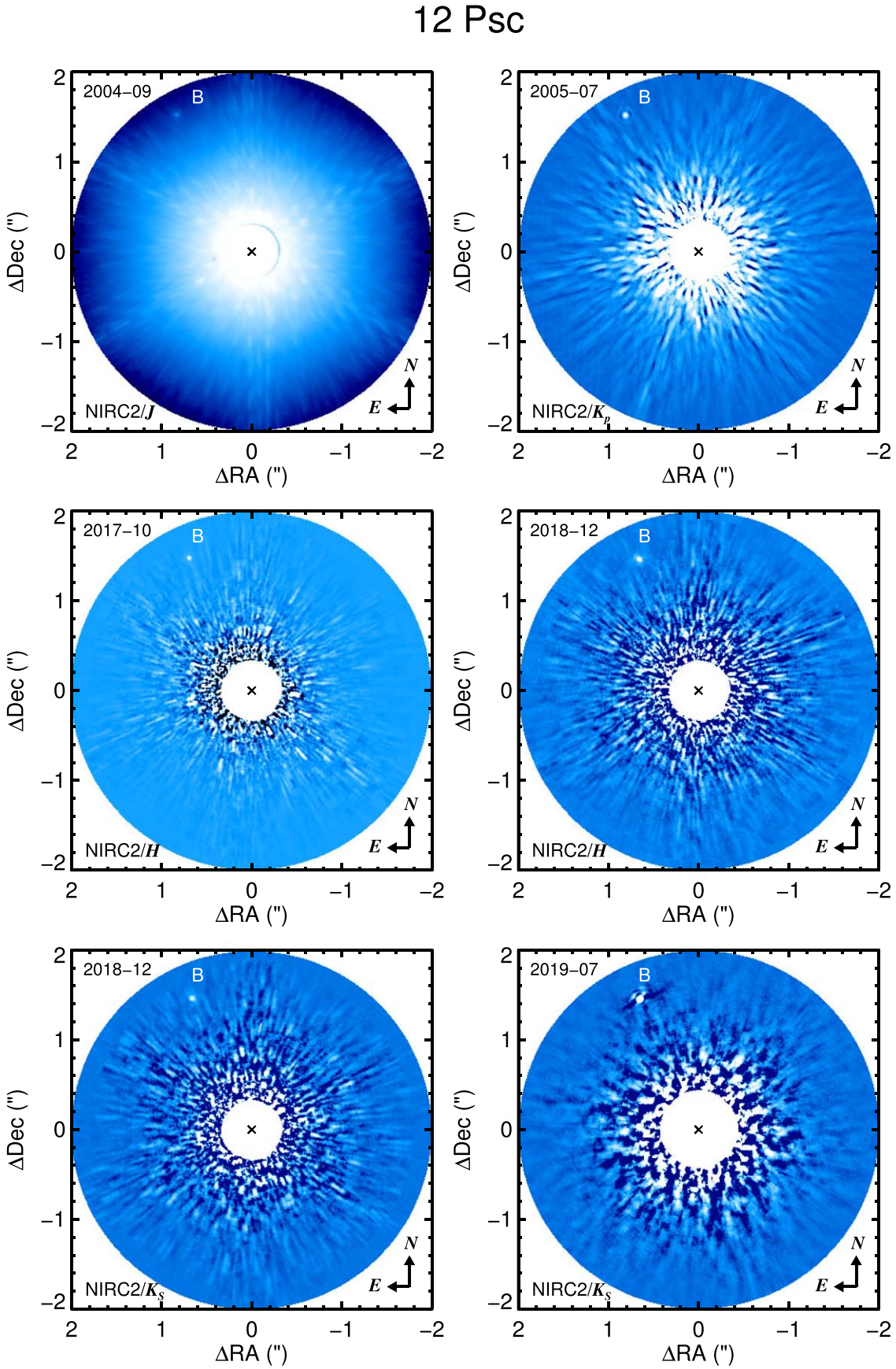

Figure 3. NIRC2 adaptive optics images of 12 Psc B between 2004 September and 2019 July. PSF subtraction has been carried out for all observations except the 2004 *J*-band data set (see Table 4 for details). The position of the host star behind the 600 mas diameter coronagraph (masked out in these images) is marked with an "×." North is up and east is to the left.

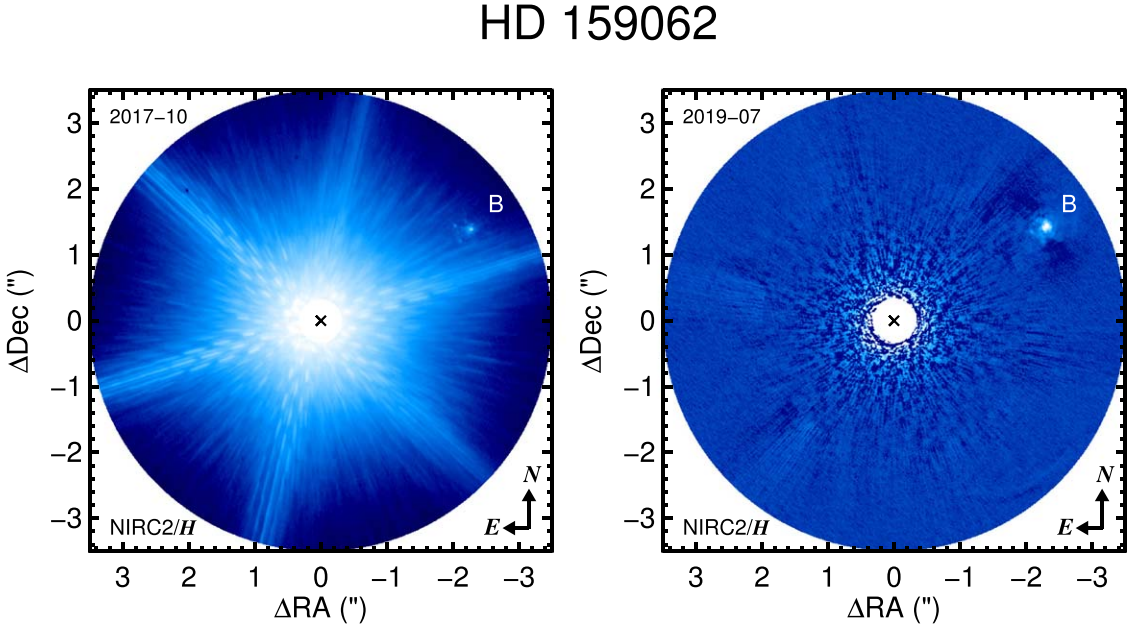

Figure 4. NIRC2 adaptive optics *H*-band observations of HD 159062 and its white dwarf companion. No additional point sources at smaller separations are evident in the post-processed 2019 July angular differential imaging sequence.

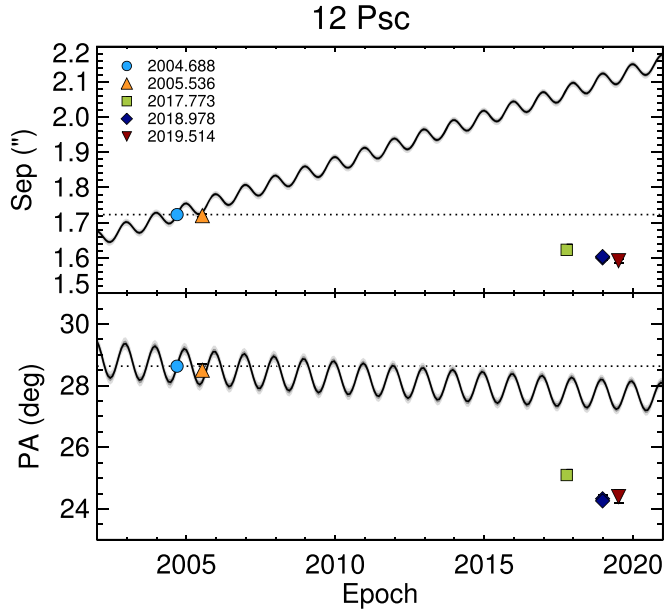

Figure 5. Relative astrometry of 12 Psc B. Based on the first imaging epoch in 2004, the separation (top panel) and position angle (bottom panel) of a stationary source would follow the background track shown in black as a result of proper and parallactic motion of the host star. 12 Psc B is clearly comoving and shows significant orbital motion.

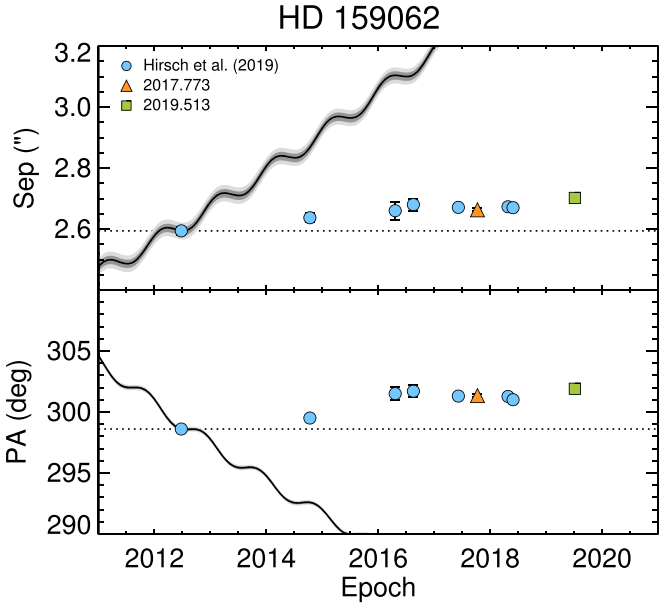

Figure 6. Same as Figure 5, but for the white dwarf HD 159062 B. Blue circles show astrometry from Hirsch et al. (2019). Our new observations in 2017 (triangle) and 2019 (square) follow a similar trend of increasing separation and position angle over time.

linear fit of the astrometry as a function of time gives a slope of -8.6 mas yr^{-1} in separation and $-0.^{\circ}30$ yr^{-1} in position angle.

Relative astrometry of HD 159062 B from Hirsch et al. (2019) and our new observations are shown in Figure 6. HD 159062 B is moving away from its host at a rate of 13.8 mas yr^{-1}. The rate of change in position angle is 0.47° yr^{-1}.

4.2. The Nature of 12 Psc B

Based solely on its brightness ($H = 15.87 \pm 0.16$ mag; $K_S = 15.93 \pm 0.2$ mag; $M_H = 13.08 \pm 0.16$ mag; $M_{K_S} = 13.1 \pm 0.2$ mag), 12 Psc B could be either a brown dwarf or a white dwarf companion. If it is a brown dwarf its absolute magnitude would imply a spectral type near the L/T transition and an H–K_S color of ≈0.6 mag (Dupuy & Liu 2012). The measured color of 12 Psc B (H–$K_S = -0.1 \pm 0.3$ mag) is significantly bluer than this, although the photometric uncertainties are large. To estimate the expected mass of the companion assuming 12 Psc B is a brown dwarf, we use a K_S-band bolometric correction from Filippazzo et al. (2015) to infer a luminosity of $\log L_{\rm bol}/L_{\odot} = -4.61 \pm 0.10$ dex. Based on the age of the host star (5.3 ± 1.1 Gyr; Soto & Jenkins 2018), substellar evolutionary models imply a mass near the hydrogen-burning limit ($77.8 \pm 1.7\,M_{\rm Jup}$ using the Burrows et al. (1997) models and $69 \pm 3\,M_{\rm Jup}$ using the Saumon & Marley (2008) hybrid models).

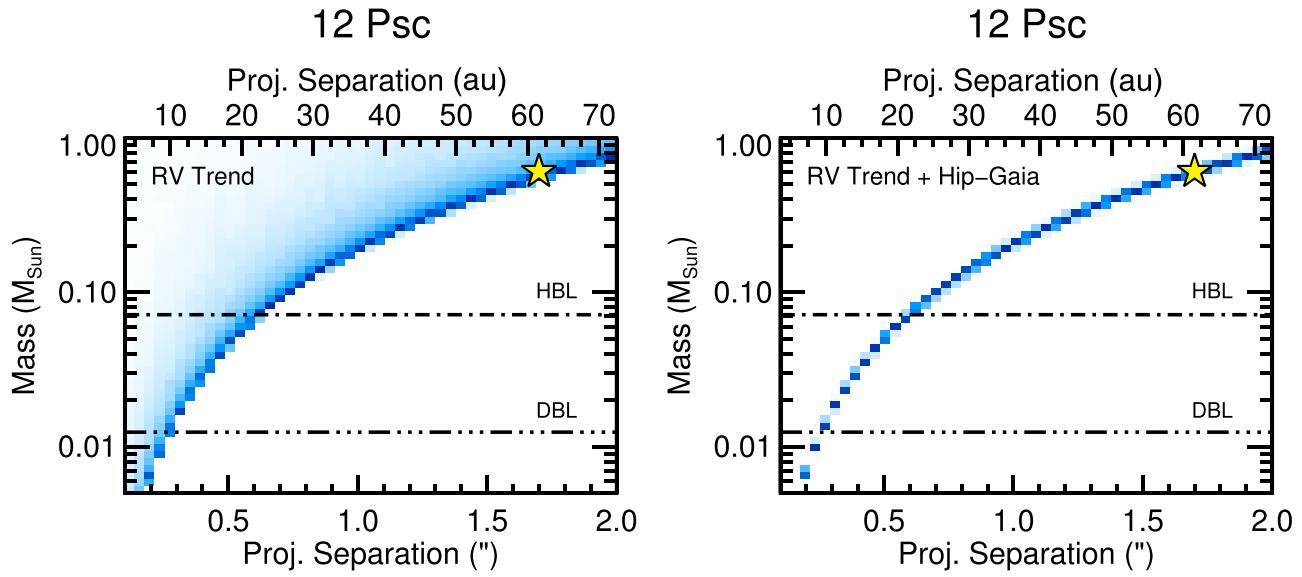

Figure 7. Joint constraints on the mass and projected separation of a companion to 12 Psc based only on the measured RV trend (left) and using both the RV trend and the astrometric acceleration (right). The hydrogen-burning limit (HBL; $\approx$75 $M_{\rm Jup}$) and deuterium-burning limit ($\approx$13 $M_{\rm Jup}$) are labeled. Based on the strength of the radial acceleration, the companion would be a brown dwarf or giant planet at close separations of $\lesssim$20 au; more massive stellar or white dwarf companions are required on wider orbits. When the HGCA acceleration is included, the range of possible masses and separations is more limited. The measured separation and dynamical mass of 12 Psc B (from Section 4.5) are shown with the star.

The slope of the RV curve and the projected separation of the companion provide direct information about the companion mass, enabling us to readily test whether this brown dwarf hypothesis for 12 Psc B is compatible with the measured radial acceleration. Following Torres (1999), the mass of a companion accelerating its host star can be derived by taking the time derivative of the RV equation of a Keplerian orbit. The companion mass (M_B) is related to the system distance (d), the projected separation of the companion (ρ), the instantaneous slope of the radial acceleration (dv_r/dt), and the orbital elements (eccentricity e, argument of periastron ω, inclination i, and Keplerian angles related to the true orbital phase—the true anomaly f and eccentric anomaly E) as

$$\frac{M_B}{M_\odot} = 5.341 \times 10^{-6}\left(\frac{d}{\rm pc}\right)^2\left(\frac{\rho}{''}\right)^2 \left|\left(\frac{dv_r/dt}{\rm m\,s^{-1}\,yr^{-1}}\right)\right. \times (1-e)(1+\cos E) \times [(1-e\cos E)\sin(f+\omega) \times (1-\sin^2(f+\omega)\sin^2 i)(1+\cos f)\sin i]^{-1}\,|. \quad (1)$$

Using only the measured RV slope, the companion mass distribution can be constrained with reasonable assumptions about the distributions of (a priori unknown) orbital elements and orbital phase angles projected on the plane of the sky. Here we adopt a uniform distribution for the argument of periastron from 0 to 2π, uniform eccentricities between 0 and 1, and an isotropic distribution of inclination angles projected on the sky (equivalent to a uniform distribution in $\cos i$). To calculate the orbital phase, a mean anomaly is randomly drawn from 0 to 2π, an eccentric anomaly is iteratively solved for using the Newton–Raphson method, and a true anomaly is computed using $\tan(f/2) = \sqrt{((1+e)/(1-e))}\tan(E/2)$. Repeating this process with Monte Carlo draws over a range of projected separations results in a joint probability distribution between the companion mass and separation based on the measured radial acceleration (and conditioned on our assumptions about the distribution of orbital elements).

Results for 12 Psc are shown in Figure 7. The measured slope of $dv_r/dt = 10.60 \pm 0.13$ m s^{-1} yr^{-1} implies that if the companion causing the acceleration was a brown dwarf or giant planet, it must be located at $\lesssim$0.″6 ($\lesssim$20 au). Assuming the RV trend originates entirely from the imaged companion we identify at 1.″6, the minimum mass of 12 Psc B is 0.49 $M_\odot$. This immediately rules out the brown dwarf scenario. It also rules out any possibility that the companion could be a low-mass star because the faintest absolute magnitude this mass threshold corresponds to is $M_{K_S} \approx 5.7$ mag following the empirical calibrations from Mann et al. (2019). This is about 10 magnitudes brighter than the observed absolute magnitude, implying that 12 Psc B must be a white dwarf.

4.3. The Nature of HD 159062 B

Following the same procedure as for 12 Psc, we show the joint mass-separation distribution for HD 159062 in Figure 8 based on our measured RV trend of $dv_r/dt = -14.1 \pm 0.3$ m s^{-1} yr^{-1}. This radial acceleration is only consistent with a brown dwarf or giant planet if the companion is located at a separation of $\lesssim$0.″9 ($\lesssim$20 au); beyond this it must be a low-mass star or a white dwarf. At a separation of 2.″7, the minimum mass implied by the radial acceleration is 0.67 $M_\odot$. However, Equation (1) assumes that the projected separation ρ and slope dv_r/dt are measured simultaneously. The mean epoch of our RV measurements is 2011.5, which is significantly earlier than our imaging observations. The closest astrometric epoch to that date from Hirsch et al. (2019) is 2012.481, at which point HD 159062 B was located at 2.″594 $\pm$ 0.″014. In Section 4.1 we found that HD 159062 B is moving away from its host at a rate of 13.8 mas yr^{-1}. If we correct for that average motion over the course of 1 year and assume a separation of 2.″580 $\pm$ 0.″014 in mid-2011, the minimum mass becomes 0.612 $\pm$ 0.015 $M_\odot$, which takes into account uncertainties in the RV trend, distance, and projected separation. Hirsch et al. (2019) and Brandt et al. (2020, submitted) analyzed observations of HD 159062 B in detail and unambiguously

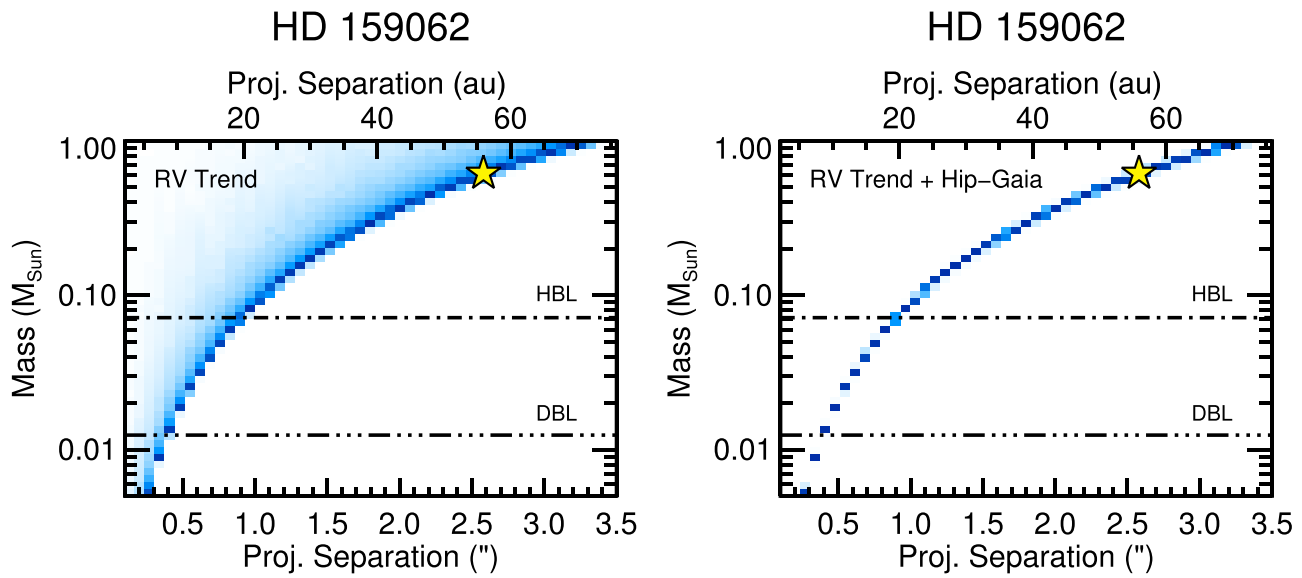

Figure 8. Same as Figure 7, but for HD 159062. The strength of the radial and astrometric accelerations together imply that the companion has a mass above the stellar limit at separations beyond about 20 au. The measured separation and dynamical mass of HD 159062 B are in good agreement with this prediction.

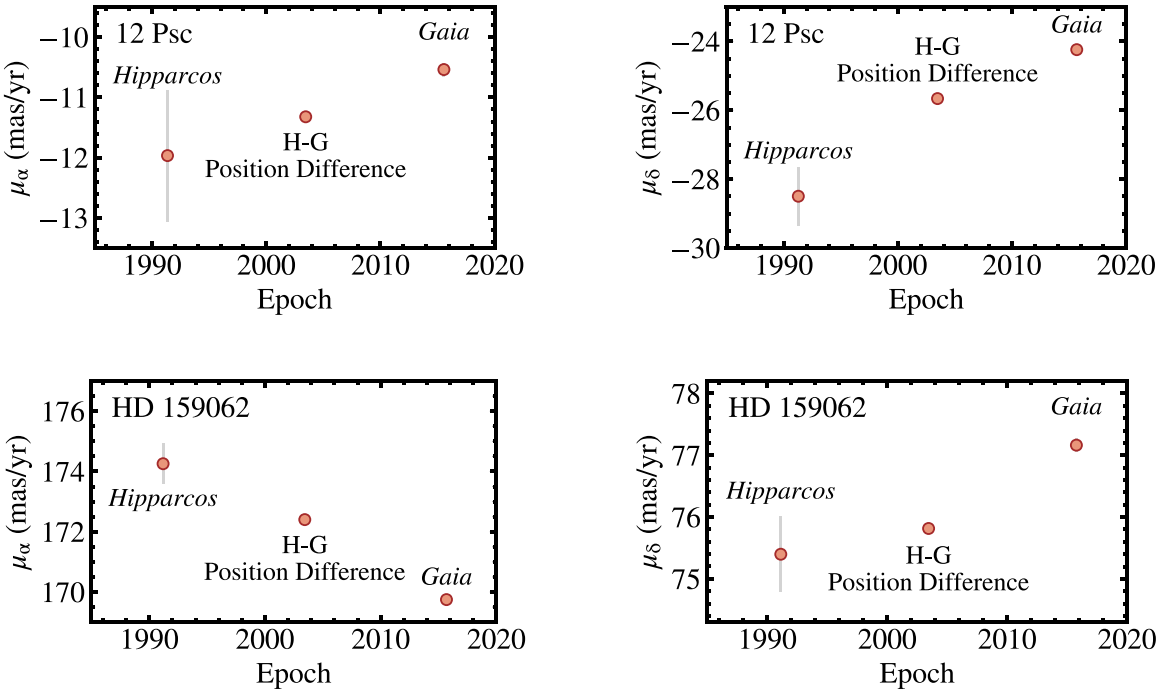

Figure 9. Proper-motion measurements from HGCA in R.A. and decl. for 12 Psc (top) and HD 159062 (bottom). Three measurements are available: the instantaneous proper motion from Hipparcos, a similar measurement from Gaia DR2, and the scaled positional difference between the two missions (see Brandt 2018 for details). Both 12 Psc and HD 159062 show clear changes in acceleration from 1991 to 2015; the slope of these proper-motion measurements represents the astrometric acceleration.

demonstrated that this companion is a white dwarf. Brandt et al. (2020, submitted) find a dynamical mass of $0.617^{+0.013}_{-0.012} M_\odot$ for HD 159062 B, which is in good agreement with our inferred minimum mass from the RV slope.

4.4. Hipparcos–Gaia Accelerations

Brandt (2018) carried out a cross-calibration between the Hipparcos and Gaia astrometric data sets which resulted in the Hipparcos–Gaia Catalog of Accelerations (HGCA). Linking these catalogs to a common reference frame (that of Gaia DR2) provides a way to correct for local sky-dependent systematics present the Hipparcos. As a result, measurements of astrometric accelerations between these two missions (separated by ≈25 yr) can be inferred through changes in proper motion. The HGCA has been an especially valuable tool to measure dynamical masses of long-period substellar companions by combining absolute accelerations with relative astrometry and RVs (Brandt et al. 2019, 2020; Dupuy et al. 2019; Franson et al., in preparation).

Both 12 Psc and HD 159062 have significant astrometric accelerations in HGCA (Figure 9). Three proper motions in

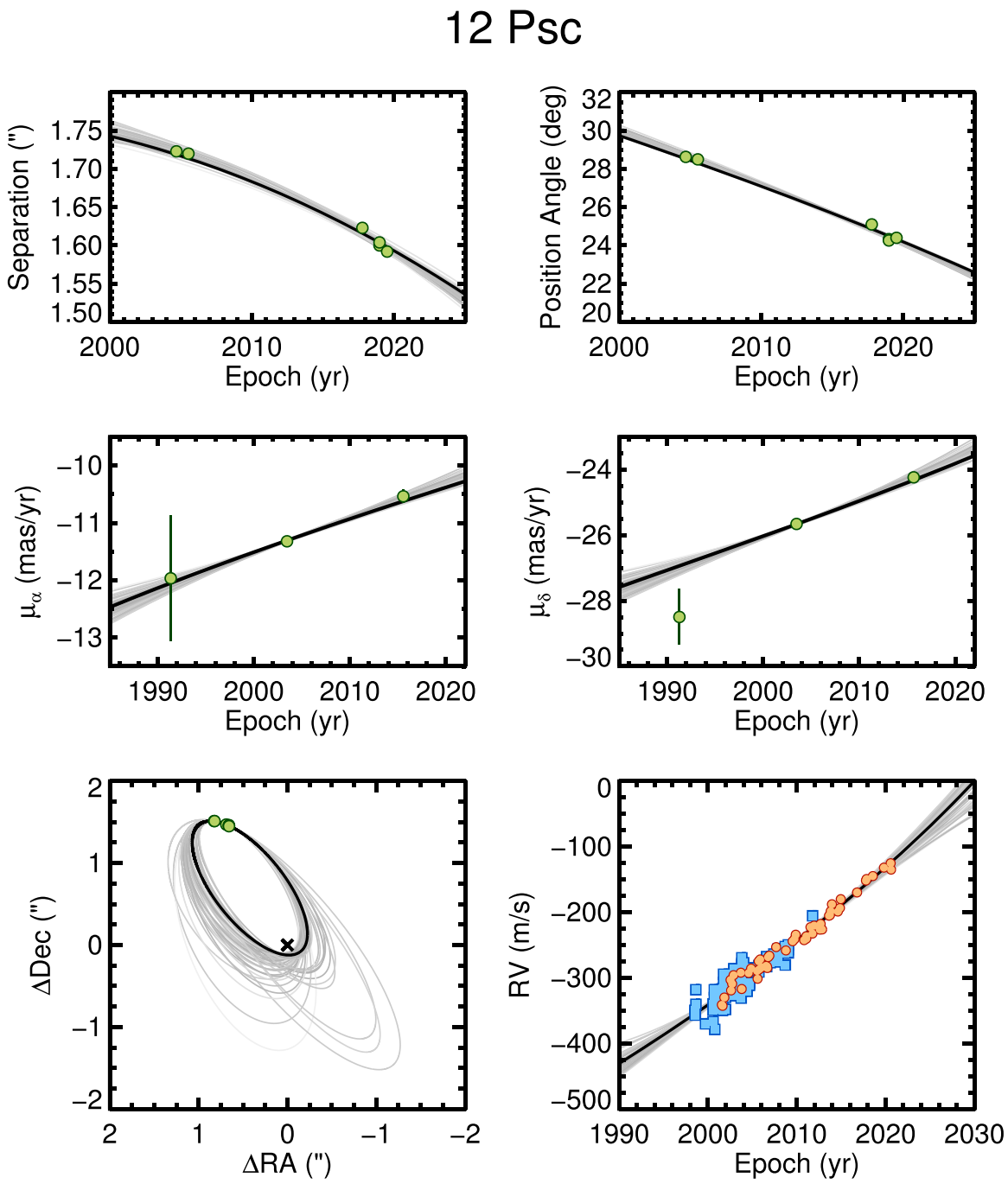

Figure 10. Keplerian orbit fit to the relative astrometry of 12 Psc B (top and lower left panels), the astrometric acceleration of the host star from the HGCA (middle panels), and RVs of 12 Psc (lower right panel). Fifty random orbits drawn from the MCMC chains are shown in gray and are color coded based on their χ^2 values; darker gray indicates a lower χ^2 value and a better fit. The best-fit orbit is shown in black. In the lower right panel, blue squares are Lick RVs and orange circles are from the Tull Spectrograph.

R.A. and decl. are available in this catalog: the proper motion in Hipparcos with a mean epoch of 1991.25, the proper motion in Gaia with a mean epoch of 2015.5, and the scaled positional difference between Hipparcos and Gaia. The latter measurement is the most precise as a result of the long baseline between the two missions.

We compute astrometric accelerations in R.A. ($d\mu_\alpha/dt$) and decl. ($d\mu_\delta/dt$) using the proper motion from Gaia and the inferred proper motion from the scaled Hipparcos–Gaia positional difference following Brandt et al. (2019): $d\mu_\alpha/dt = 2\ \ \Delta\mu_{\alpha,\mathrm{Gaia-HG}}/(t_{\alpha,\mathrm{Gaia}} - t_{\alpha,\mathrm{Hip}})$ and $d\mu_\delta/dt = 2\ \Delta\mu_{\delta,\mathrm{Gaia-HG}}/(t_{\delta,\mathrm{Gaia}} - t_{\delta,\mathrm{Hip}})$. Here $t_{\alpha,\mathrm{Gaia}}$ and $t_{\delta,\mathrm{Gaia}}$ are the Gaia astrometric epochs corresponding to the proper-motion measurements in R.A. and decl., and $t_{\alpha,\mathrm{Hip}}$ and $t_{\delta,\mathrm{Hip}}$ are the corresponding epochs for Hipparcos. The total acceleration is then computed as $d\mu_{\alpha\delta}/dt = \sqrt{(d\mu_\alpha/dt)^2 + (d\mu_\delta/dt)^2}$.

Brandt et al. (2019) presented a simple relationship between the mass of a companion (M_B), its instantaneous projected separation (ρ), and both the radial (dv_r/dt) and astrometric ($d\mu_{\alpha\delta}/dt$) accelerations induced on its host star. In convenient

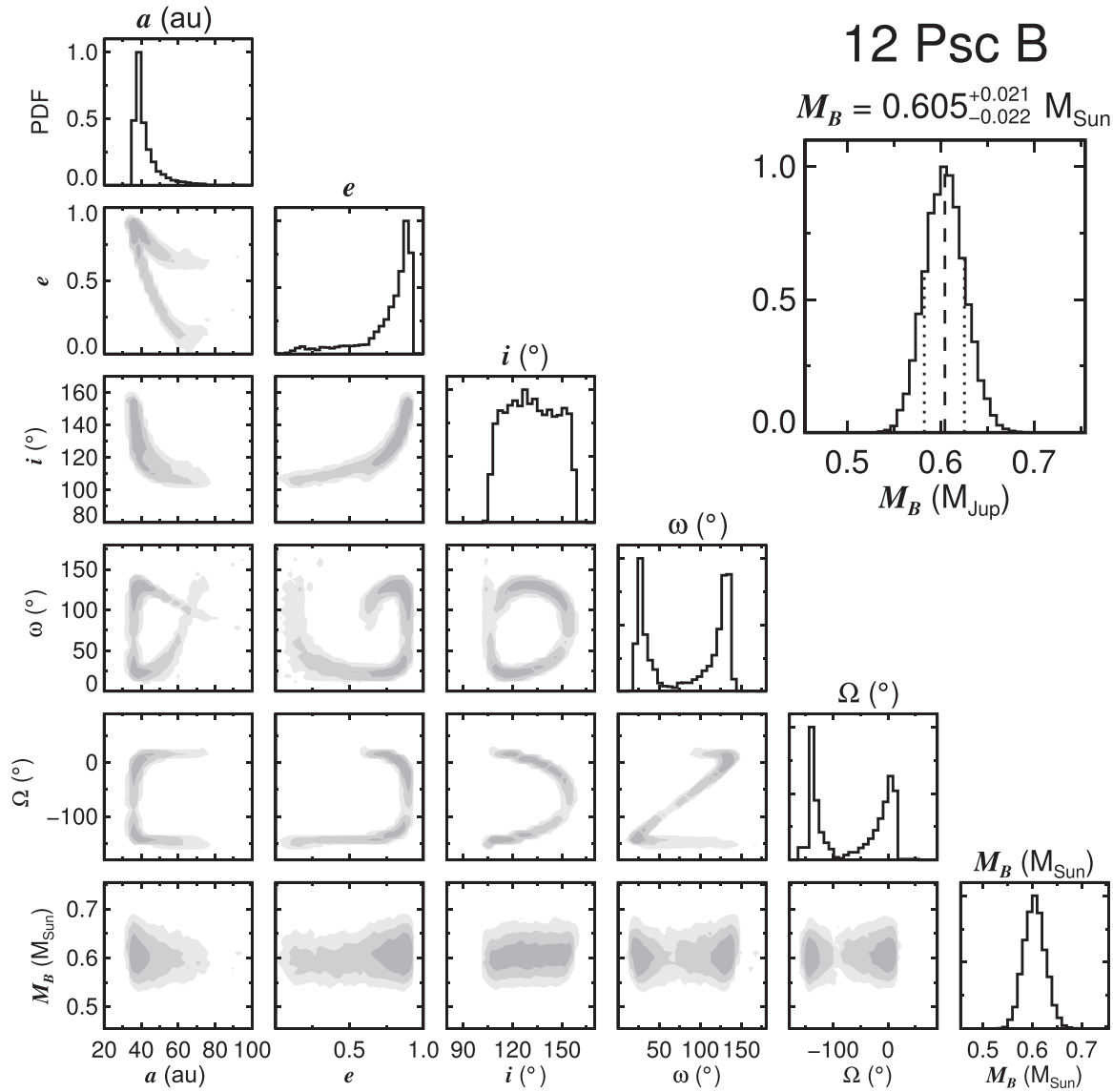

Figure 11. Corner plot showing joint posterior maps of various parameters and their marginalized probability density functions. The observations of 12 Psc B and its host star favor a high-eccentricity orbit and a semimajor axis of ≈40 au. The dynamical mass of the white dwarf companion 12 Psc B is $0.605^{+0.021}_{-0.022}\,M_{\odot}$.

units this can be expressed as

$$\frac{M_B}{M_{\rm Jup}} = 5.599 \times 10^{-3}\left(\frac{d}{\rm pc}\right)^2\left(\frac{\rho}{''}\right)^2\left[\left(\frac{d\mu_{\alpha\delta}/dt}{\rm m\,s^{-1}\,yr^{-1}}\right)^2 + \left(\frac{dv_r/dt}{\rm m\,s^{-1}\,yr^{-1}}\right)^2\right]^{3/2}\left(\frac{d\mu_{\alpha\delta}/dt}{\rm m\,s^{-1}\,yr^{-1}}\right)^{-2}. \quad (2)$$

The numerical coefficient becomes 5.342×10^{-6} when M_B is in units of $M_{\odot}$. Equation (2) is valid when all three measurements (ρ, dv_r/dt, and $d\mu_{\alpha\delta}/dt$) are obtained simultaneously. This is rarely the case in practice, but this relation offers a convenient approximation of the dynamical mass as long as the orbit has not evolved substantially, as is the case for long-period companions.

The HGCA kinematics for 12 Psc are listed in Table 1 and displayed in Figure 9. 12 Psc shows a significant change in proper motion between the Hipparcos and Gaia scaled positional difference and Gaia measurements: $\Delta\mu_{\alpha,\rm Gaia-HG} = 0.78 \pm 0.12$ mas yr^{-1} and $\Delta\mu_{\delta,\rm Gaia-HG} = 1.42 \pm 0.09$ mas yr^{-1}. This translates into an astrometric acceleration of $d\mu_{\alpha\delta}/dt = 22.9 \pm 1.4$ m s^{-1} yr^{-1}—about twice as large as its radial acceleration. The inferred constraints on the companion mass and separation resulting from these radial and astrometric accelerations are shown in Figure 7. The projected separation of 12 Psc ranges from 1.″723 in 2004 to 1.″592 in 2019. Using a projected separation of $\rho = 1.''7$, which is closer to the midpoints of the radial and astrometric accelerations, Equation (2) implies a mass of about $0.622 \pm 0.018\,M_{\odot}$. This is typical of white dwarf masses (e.g., Kepler et al. 2007).

HD 159062 also shows substantial changes in proper motion in the HGCA (Figure 9): $\Delta\mu_{\alpha,\rm Gaia-HG} = -2.66 \pm 0.12$ mas yr^{-1} and $\Delta\mu_{\delta,\rm Gaia-HG} = 1.35 \pm 0.11$ mas yr^{-1}. This translates into an astrometric acceleration of $d\mu_{\alpha\delta}/dt = 25.0 \pm 1.0$ m s^{-1} yr^{-1}. Figure 8 shows constraints combining this with the RV trend. At

Table 5
12 Psc B Orbital Fit Results

Parameter	Prior	Best Fit	Median	MAP[a]	68.3% CI	95.4% CI
			Fitted Parameters			
M_1 ($M_\odot$)	$\mathcal{N}(1.1,0.2)$	1.10	1.10	1.07	(0.91, 1.31)	(0.70, 1.51)
M_2 ($M_\odot$)	$1/M_2$	0.594	0.605	0.594	(0.583, 0.625)	(0.564, 0.648)
a (AU)	$1/a$	38.8	39.5	37.5	(36.0, 42.3)	(35.4, 57.7)
$\sqrt{e}\sin\omega$	$\mathcal{U}(-1,1)$	0.70	0.65	0.68	(0.30, 0.74)	(0.29, 0.96)
$\sqrt{e}\cos\omega$	$\mathcal{U}(-1,1)$	−0.63	−0.20	0.78	(−0.68, 0.65)	(−0.67, 0.81)
i (°)	sin$i$	140	132	123	(118, 151)	(108, 157)
Ω (°)	$\mathcal{U}(-180, 180)$	−4.77	−42.2	−142	(−145, −7.2)	(−145, 13.3)
$\lambda_{\rm ref}$ (°)[b]	$\mathcal{U}(-180, 180)$	17.9	−23.3	34.5	(−125, 42.4)	(−163, 45.9)
			Derived Parameters			
e	⋯	0.89	0.84	0.89	(0.76, 0.92)	(0.27, 0.93)
ω (°)	⋯	132	104	25.5	(33.9, 138)	(22.0, 138)
P (yr)	⋯	186	193	175	(155, 218)	(145, 348)
τ (yr)[c]	⋯	2069	2074	2070	(2060, 2080)	(2060, 2180)
d_p (AU)	⋯	4.5	6.4	3.5	(2.7, 10.2)	(2.4, 40.2)
d_a (AU)	⋯	73.2	71.2	68.5	(66.9, 73.9)	(66.2, 85.1)

Notes.
[a] Maximum a posteriori probability.
[b] Mean longitude at the reference epoch, 2455197.5 JD.
[c] Time of periastron, 2455197.5 JD—$P(\lambda_{\rm ref}-\omega)/(2\pi)$.

a separation of $2\farcs580 \pm 0.014$ mas, the implied mass HD 159062 B is $0.632 \pm 0.014\,M_\odot$—in good agreement with the dynamical mass. Below we carry out a full orbit fit of 12 Psc B and HD 159062 B using relative astrometry, RVs, and absolute astrometry from the HGCA.

4.5. Orbit and Dynamical Mass of 12 Psc B

The orbit and dynamical mass of 12 Psc B are determined using the efficient orbit fitting package `orvara` (Brandt et al. 2020, submitted), which jointly fits Keplerian orbits to RVs, relative astrometry of resolved companions, and absolute astrometry from HGCA. The code relies on a Bayesian framework with the `emcee` affine-invariant implementation of Markov Chain Monte Carlo (MCMC; Foreman-Mackey et al. 2013) to sample posterior distributions of orbital elements, physical parameters of the host and companion, and nuisance parameters like stellar parallax, instrument-dependent RV offsets, and RV jitter. We use 100 walkers with 10^5 steps for our orbital fit of the 12 Psc system.

Our priors are chosen to ensure that the observations drive the resulting posteriors. We adopt log-flat priors for the semimajor axis, companion mass, and RV jitter; a $\sin i$ distribution for inclination; and linearly uniform priors for all other fitted parameters ($\sqrt{e}\sin\omega$, $\sqrt{e}\cos\omega$, longitude of ascending node, and longitude at a reference epoch). A Gaussian prior with a mean of 1.1 $M_\odot$ and a standard deviation of 0.2 $M_\odot$ is chosen for the primary mass based on independent estimates from the literature (e.g., $1.11 \pm 0.05\,M_\odot$, Soto & Jenkins (2018); $1.079 \pm 0.012\,M_\odot$, Tsantaki et al. 2013; $1.12 \pm 0.08\,M_\odot$, Mints & Hekker 2017).

Results of the orbital fit for 12 Psc B are shown in Figures 10 and 11.[10] The orbit of 12 Psc B has a high eccentricity of 0.84 ± 0.08, an orbital period of 193^{+25}_{-38} yr, and a semimajor axis of $39.5^{+2.8}_{-3.5}$ au. The dynamical mass of 12 Psc B is $0.605^{+0.021}_{-0.022}\,M_\odot$, which is similar to our mass estimate in Section 4.4 using simplifying assumptions. A summary of prior and posterior distributions for relevant fitted parameters can be found in Table 5.

4.6. Orbit and Dynamical Mass of HD 159062 B

We fit a Keplerian orbit using `orvara` jointly to our HRS RVs, our new NIRC2 astrometry, and the HGCA acceleration for HD 159062 together with HIRES RVs and relative astrometry from Hirsch et al. (2019). The same priors we used for 12 Psc B in Section 4.5 are adopted for HD 159062 B except for the host star mass. For this we use a Gaussian prior with a mean of 0.8 $M_\odot$ and a standard deviation of 0.2 $M_\odot$, which captures the typical range of mass estimates for HD 159062 from the literature (e.g., $0.76 \pm 0.03\,M_\odot$, Hirsch et al. 2019; $0.78 \pm 0.03\,M_\odot$, Mints & Hekker 2017; $0.87\,M_\odot$, Luck 2017).

Results of the orbit fit are shown in Figures 12 and 13, and a summary of the posterior distributions is listed in Table 6. The dynamical mass of HD 159062 B is $0.609^{+0.010}_{-0.011}\,M_\odot$, which happens to be very similar to the mass we found for 12 Psc B. HD 159062 B orbits with a semimajor axis of 60^{+5}_{-7} au, a period of 390 ± 70 yr, and a low eccentricity which peaks at $e = 0.0$ and is below $e = 0.42$ with 95% confidence. These are consistent with but more precise than the values found by Hirsch et al. (2019) and Brandt et al. (2020, submitted).

Our dynamical mass of $0.609^{+0.010}_{-0.011}M_\odot$ is somewhat lower than the value of $0.65^{+0.12}_{-0.04}M_\odot$ from Hirsch et al. (2019) and $0.617^{+0.013}_{-0.012}M_\odot$ from Brandt et al. (2020, submitted). Because the mass of white dwarf remnants scales strongly with progenitor mass, a lower final mass implies a substantially lower initial mass (and longer main-sequence lifetime) compared to the 2.4 $M_\odot$ progenitor mass found by Hirsch et al. (2019). The

[10] Note that the parameter values for orbital fits quoted in this study represent the median of the parameter posterior distributions and the 68.3% credible interval, although we also list the best-fit values and the maximum a posteriori probabilities in Table 5.

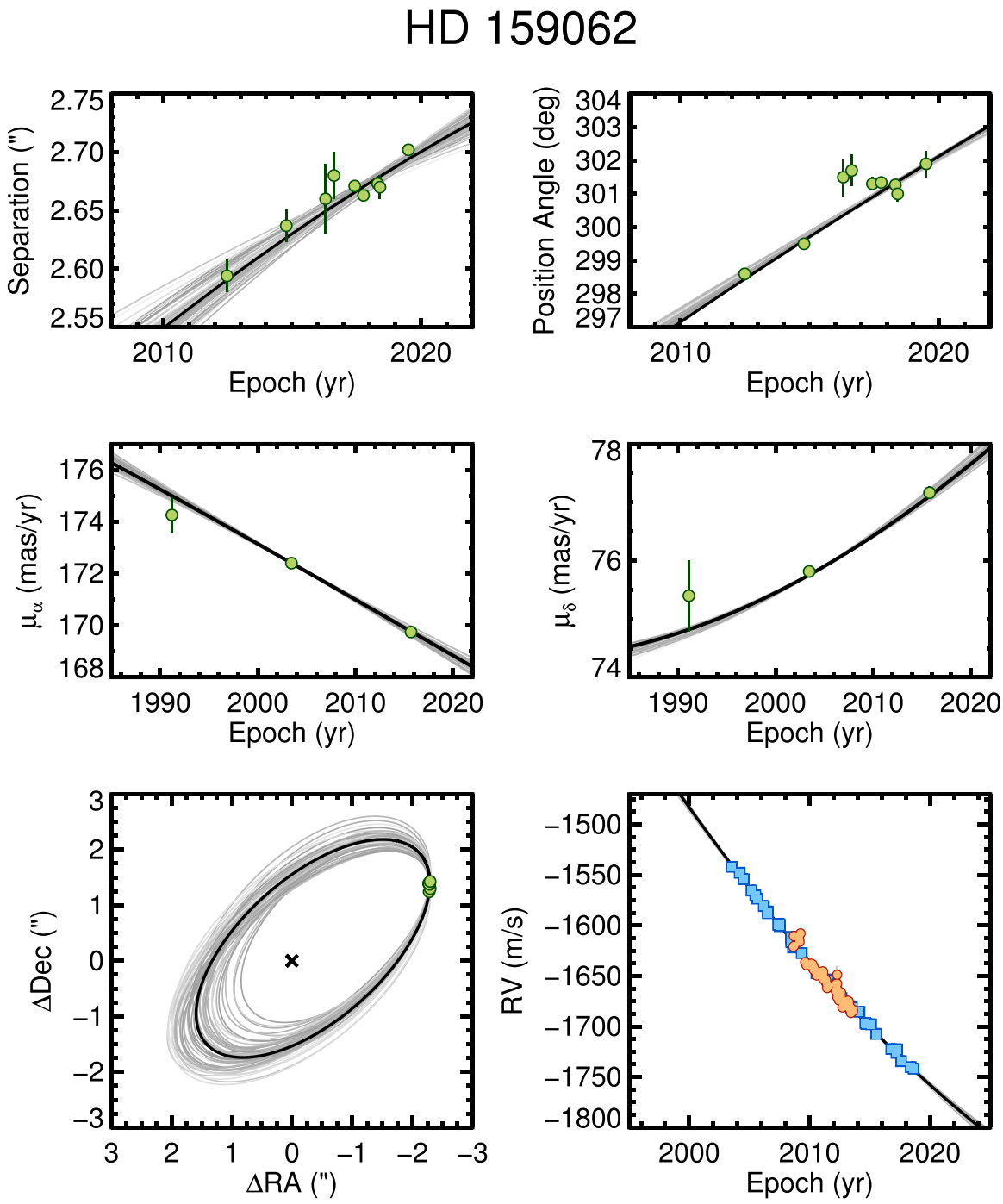

Figure 12. Keplerian orbit fit for HD 159062 B from relative astrometry (top), astrometric acceleration from HGCA (middle panels), and RVs (bottom right). See Figure 10 for details. In the lower right panel, our RVs from HRS are shown as orange circles while HIRES RVs from Hirsch et al. (2019) are shown as blue squares.

implications of a lower progenitor mass are discussed in more detail below.

5. Discussion and Conclusions

Stars with masses $\lesssim 8\,M_\odot$ evolve to become white dwarfs on timescales of a few tens of megayears for high-mass stars near the threshold for core-collapse supernovae (e.g., Ekstrom et al. 2012; Burrows 2013) to $\sim 10^4$ Gyr for the lowest-mass stars near the hydrogen-burning limit (Laughlin et al. 1997). Given the 13.8 Gyr age of the universe, the lowest-mass stars that could have evolved in isolation to become white dwarfs have masses of ≈ 0.9–$1\,M_\odot$. White dwarf masses generally increase with progenitor mass, and the corresponding minimum white dwarf mass that can result from isolated evolution of such a star at solar metallicity is $\gtrsim 0.56\,M_\odot$ (Cummings et al. 2018). Most white dwarfs should therefore have masses above this value, and indeed the peak of the white dwarf mass function in the solar neighborhood is $\approx 0.6\,M_\odot$ (e.g., Liebert et al. 2005; Kepler et al. 2007). The majority of these have hydrogen atmospheres with DA classifications (Kepler et al. 2007).

The initial-to-final mass relation connects a progenitor star's mass to the final mass of the resulting white dwarf remnant.

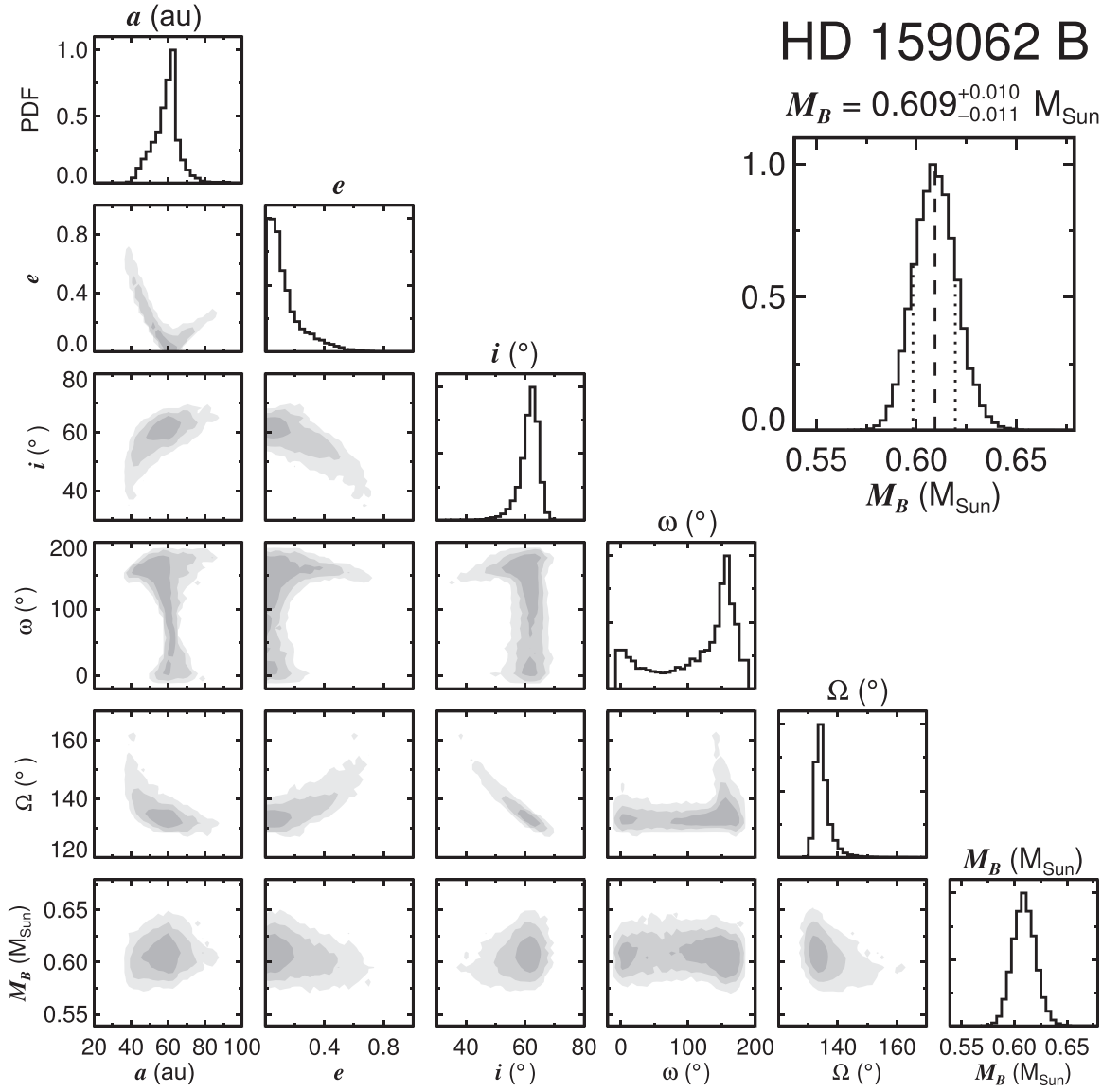

Figure 13. Same as Figure 11, but for HD 159062 B. The dynamical mass of the white dwarf companion HD 159062 B is $0.609^{+0.010}_{-0.011}\,M_{\odot}$.

These relations are sensitive to metallicity and the physics of AGB evolution, including shell burning, dedge-up events, and mass loss (e.g., Marigo & Girardi 2007). Cummings et al. (2018) provide a semi-empirical calibration of the white dwarf initial-to-final mass relation spanning initial masses of $\approx$0.9–7 $M_{\odot}$ or final masses between $\approx$0.5 and 1.2 $M_{\odot}$. Using this relation, our dynamical mass measurements for the white dwarfs 12 Psc B and HD 159062 B imply nearly identical initial progenitor masses of $1.5 \pm 0.6\,M_{\odot}$ for both companions. The large uncertainties reflect the significant scatter in the empirically calibrated initial-to-final mass relation, which is sparsely populated for initial masses $\lesssim$2.5 $M_{\odot}$. Theoretical stellar evolutionary models also exhibit substantial dispersion in the initial-to-final mass relation, with initial masses predicted to be between $\approx$1.3 and 2.2 $M_{\odot}$ at solar metallicity for the final masses we measure for 12 Psc B and HD 159062 B (e.g., Marigo & Girardi 2007; Choi et al. 2016).

The 12 Psc system was therefore initially a $\sim 1.5\,M_{\odot} + 1.1\,M_{\odot}$ binary and the HD 159062 system was initially a $\sim 1.5\,M_{\odot} + 0.8\,M_{\odot}$ binary. The more massive components then underwent standard evolution through the giant and AGB phases. At this point, after about 2.9 Gyr of evolution, their radii expanded to $\sim$450 $R_{\odot}$ ($\sim$2.1 au) before shedding $\approx$60% of their initial mass to become white dwarfs (Paxton et al. 2010; Choi et al. 2016; Dotter 2016; Cummings et al. 2018). Adopting an age of 5.3 ± 1.1 Gyr for 12 Psc from Soto & Jenkins (2018), the most likely companion progenitor mass of $\sim 1.5\,M_{\odot}$ implies that the cooling age of 12 Psc B is $\sim$2–3 Gyr. A higher (lower) progenitor mass would result in a longer (shorter) cooling age. The age of HD 159062 is somewhat more uncertain, but for a system age of $\sim$9–13 Gyr, a main-sequence lifetime of $\approx$3 Gyr for the progenitor of HD 159062 B implies a cooling time of $\sim$6–10 Gyr for the white dwarf. This is consistent with the cooling age of $8.2^{+0.3}_{-0.5}$ Gyr derived by Hirsch et al. (2019).

Despite both binaries having broadly similar physical characteristics, it is interesting to note the differences in the orbits of these companions. 12 Psc B has a high eccentricity of $e = 0.84 \pm 0.08$ and a semimajor axis of 40^{+2}_{-4} au, which takes it to a periastron distance of 6.4 au (with a 68% credible interval spanning 2.7–10.2 au). On the other hand, HD 159062 B has a

Table 6
HD 159062 B Orbital Fit Results

Parameter	Prior	Best Fit	Median	MAP[a]	68.3% CI	95.4% CI
			Fitted Parameters			
M_1 ($M_\odot$)	$\mathcal{N}(0.8,0.2)$	0.896	0.799	0.770	(0.62, 0.97)	(0.46, 1.16)
M_2 ($M_\odot$)	$1/M_2$	0.597	0.609	0.610	(0.599, 0.619)	(0.588, 0.630)
a (AU)	$1/a$	62.3	59.9	62.5	(52.7, 65.0)	(42.7, 71.0)
$\sqrt{e}\sin\omega$	$\mathcal{U}(-1,1)$	0.021	−0.14	−0.20	(−0.30, −0.02)	(−0.35, 0.18)
$\sqrt{e}\cos\omega$	$\mathcal{U}(-1,1)$	0.11	0.18	0.28	(−0.07, 0.48)	(−0.36, 0.64)
i (°)	sin$i$	64.6	61.9	62.3	(59.5, 64.9)	(54.1, 67.1)
Ω (°)	$\mathcal{U}(-180, 180)$	133	134	134	(132, 140)	(130, 141)
$\lambda_{\rm ref}$ (°)[b]	$\mathcal{U}(-180, 180)$	146	147	148	(141, 155)	(125, 161)
			Derived Parameters			
e	···	0.013	0.092	0.010	(0.00, 0.15)	(0.00, 0.40)
ω (°)	···	10.7	139	156	(103, 180)	(8.21, 180)
P (yr)	···	402	387	407	(314, 457)	(230, 533)
τ (yr)[c]	···	1858	2000	2025	(1950, 2050)	(1840, 2050)
d_p (AU)	···	61	56	63	(49, 64)	(28, 64)
d_a (AU)	···	63	64	64	(62, 65)	(62, 78)

Notes.
[a] Maximum a posteriori probability.
[b] Mean longitude at the reference epoch, 2455197.5 JD.
[c] Time of periastron, 2455197.5 JD—$P(\lambda_{\rm ref}-\omega)/(2\pi)$.

Table 7
Resolved Sirius-Like White Dwarf Companions with Dynamical Mass Measurements

Name	Dynamical Mass ($M_\odot$)	White Dwarf SpT	Host Star SpT	Proj. Sep.[a] (″)	a (AU)	System Age (Gyr)	WD Cooling Age (Gyr)	Ref.
40 Eri B	0.573 ± 0.018	DA2.9	M4.5+K0	8.3	35	≈1.8	≈0.122	1, 2 , 3
Procyon B	0.592 ± 0.006	DQZ	F5 IV–V	3.8	15	∼2.7	1.37 ± 0.04	4
Gl 86 B	0.596 ± 0.010	DQ6	K0 V	2.4	22	∼2.5	1.25 ± 0.05	5, 6
12 Psc B	$0.605^{+0.021}_{-0.022}$	···	G1 V	1.6	40	5.3 ± 1.1	∼2–3	7
HD 159062 B	$0.609^{+0.010}_{-0.011}$	···	G9 V	2.7	60	∼9–13	8^{+3}_{-5}	7, 8
Stein 2051 B[b]	0.675 ± 0.051	DC	M4	10.1	56	1.9–3.6	1.9 ± 0.4	9
Sirius B	1.018 ± 0.011	DA2	A1 V	10.7	20	0.288 ± 0.010	≈0.126	10

Notes. Entries in this table are limited to white dwarf companions with precise dynamical mass constraints ($\sigma_M/M < 10\%$).
[a] Most recently reported projected separation.
[b] The mass of Stein 2051 B was measured via gravitational deflection.
References: (1) Gianninas et al. (2011); (2) Mason et al. (2017); (3) Bond et al. (2017a); (4) Bond et al. (2015); (5) Farihi et al. (2013); (6) Brandt et al. (2019); (7) this work; (8) Hirsch et al. (2019); (9) Sahu et al. (2017); (10) Bond et al. (2017b).

low eccentricity most consistent with a circular orbit ($e < 0.42$ at 95% confidence), a semimajor axis of 60^{+5}_{-7} au, and a periastron distance of 56^{+8}_{-7} au. Given the orbital properties of 12 Psc B, tidal interactions during the AGB phase should have been important for this system. Without other mechanisms to increase eccentricities, these interactions tend to dampen eccentricities and reduce orbital periods (e.g., Saladino & Pols 2019). Bonačić Marinović et al. (2008) highlight Sirius as an example of a binary which began as a $\sim 2.1 + 5.5\,M_\odot$ pair which should have circularized, but Sirius B now orbits with an eccentricity of $e = 0.59$ and an orbital period of 50 yr. Assuming a mass ratio of $q = M_1/M_2 \sim 1.4$ for the unevolved 12 Psc system, the Roche lobe for the 12 Psc B progenitor would have been ≈2.6 au at periastron following the approximation for the Roche lobe effective radius from Eggleton (1983). This is comparable to the size of 12 Psc B during the AGB phase (∼2.1 au). Mass transfer via Roche lobe overflow may therefore have occurred in this system, and tidal interactions would have been important. Like the Sirius system, the high eccentricity of 12 Psc B is therefore surprising and lends support to an eccentricity pumping mechanism, perhaps through enhanced mass loss at periastron which may counteract tidal circularization (Bonačić Marinović et al. 2008).

Wide companions will evolve as if in isolation whereas short-period systems will evolve through one of several channels as detached, semi-detached, or contact binaries. 12 Psc B and HD 159062 B occupy an intermediate regime at several tens of astronomical units where direct mass transfer via Roche lobe overflow may not have occurred, but wind accretion could have been important as a source of chemical enrichment of the unevolved companion as each progenitor underwent mass loss. This is especially true for HD 159062, which shows an enhanced abundance of barium and other *s*-process elements—a signpost of prior accretion from an AGB companion (e.g., McClure et al. 1980; Escorza et al. 2019). For

example, Fuhrmann et al. (2017) found a barium abundance of $[Ba/Fe] = +0.40 \pm 0.01$ dex, and Reddy et al. (2006) found $[Y/Fe] = +0.37$ dex, $[Ce/Fe] = +0.10$ dex, and $[Nd/Fe] =$ 0.39 dex. This led Fuhrmann et al. (2017) to predict that HD 159062 harbors a white dwarf companion, which was later confirmed with the discovery of HD 159062 B by Hirsch et al. (2019).

On the other hand, 12 Psc shows no signs of barium enrichment or significant enrichment from other *s*-process elements: Delgado Mena et al. (2017) found abundances of $[Ba/Fe] = -0.03 \pm 0.02$ dex, $[Sr/Fe] = +0.12 \pm 0.03$ dex, $[Y/Fe] = +0.09 \pm 0.04$ dex, $[Zr/Fe] = +0.01 \pm 0.08$ dex, $[Ce/Fe] = -0.07 \pm 0.04$ dex, and $[Nd/Fe] = -0.09 \pm 0.03$ dex. This lack of enrichment is surprising when compared to HD 159062: both have white dwarf companions with similar masses and presumably similar evolutionary pathways for their progenitors, but 12 Psc B is on a highly eccentric orbit which brings it much closer to its unevolved main-sequence companion at periastron (≈6 au for 12 Psc B versus ≈56 au for HD 159062 B). Given that most barium stars have companions with orbital periods $\lesssim 10^4$ days (e.g., McClure et al. 1980), that would naturally lead to the expectation that 12 Psc should be even more enriched compared to HD 159062 because of more efficient accretion at periastron. This raises two open questions for the 12 Psc system: why was 12 Psc B not tidally circularized during the AGB phase? Why is 12 Psc unenriched in barium and *s*-process elements? The chemical peculiarities of some barium stars have been attributed to winds from former AGB companions (now white dwarfs) on orbits out to several thousand astronomical units (De Mello & da Silva 1997). It remains unclear why some stars with white dwarf companions at moderate separations appear to have normal abundances while others show various patterns of enrichment. The answer may involve convection and dissipation of material from the host star, the amount of mass lost from the AGB companion, or perhaps a third evolved (and now engulfed) companion in the system.

12 Psc B and HD 159062 B join a small but growing list of directly imaged white dwarf companions with measured dynamical masses orbiting main-sequence stars. To our knowledge, only seven systems with resolved white dwarf companions and precise dynamical mass measurements are known (including 12 Psc B and HD 159062 B; see the compilation in Table 7). These Sirius-like benchmark systems are valuable because they can be directly characterized with photometry and spectroscopy—yielding an effective temperature, bolometric luminosity, radius, and spectral classification—and the total system age and progenitor metallicity can be determined from the host star. These combined with a mass measurement provide fundamental tests of white dwarf mass–radius relations and cooling models (e.g., Bond et al. 2017b; Bond et al. 2017a; Serenelli et al. 2020). Follow-up spectroscopy and multiwavelength photometry of 12 Psc B and HD 159062 B are needed to better characterize these companions and carry out robust tests of cooling models.

The authors are grateful to Michal Liu for the early NIRC2 imaging observations of 12 Psc in 2004 and 2005 as well as Keith Hawkins for helpful discussions about this system. We thank Diane Paulson, Rob Wittenmyer, Erik Brugamyer, Caroline Caldwell, Paul Robertson, Kevin Gullikson, and Marshall Johnson for contributing to the Tull observations of 12 Psc presented in this study. This work was supported by a NASA Keck PI Data Award, administered by the NASA Exoplanet Science Institute. Data presented herein were obtained at the W. M. Keck Observatory from telescope time allocated to the National Aeronautics and Space Administration through the agency's scientific partnership with the California Institute of Technology and the University of California. The Observatory was made possible by the generous financial support of the W. M. Keck Foundation. This research has made use of the Keck Observatory Archive (KOA), which is operated by the W. M. Keck Observatory and the NASA Exoplanet Science Institute (NExScI), under contract with the National Aeronautics and Space Administration. B.P.B. acknowledges support from the National Science Foundation grant AST-1909209. The authors wish to recognize and acknowledge the very significant cultural role and reverence that the summit of Maunakea has always had within the indigenous Hawaiian community. We are most fortunate to have the opportunity to conduct observations from this mountain.

Facilities: Smith (Tull Spectrograph), HET (HRS), Keck:II (NIRC2).

ORCID iDs

Brendan P. Bowler https://orcid.org/0000-0003-2649-2288
William D. Cochran https://orcid.org/0000-0001-9662-3496
Michael Endl https://orcid.org/0000-0002-7714-6310
Timothy D. Brandt https://orcid.org/0000-0003-2630-8073
Trent J. Dupuy https://orcid.org/0000-0001-9823-1445
Kaitlin M. Kratter https://orcid.org/0000-0001-5253-1338
Dimitri Mawet https://orcid.org/0000-0002-8895-4735
Garreth Ruane https://orcid.org/0000-0003-4769-1665

References

Aguilera-Gómez, C., Ramírez, I., & Chanamé, J. 2018, A&A, 614, A55
Bonačić Marinović, A. A., Glebbeek, E., & Pols, O. R. 2008, A&A, 480, 797
Bond, H. E., Bergeron, P., & Bédard, A. 2017a, ApJ, 848, 16
Bond, H. E., Gilliland, R. L., Schaefer, G. H., et al. 2015, ApJ, 813, 106
Bond, H. E., Schaefer, G. H., Gilliland, R. L., et al. 2017b, ApJ, 840, 70
Bowler, B. P. 2016, PASP, 128, 102001
Bowler, B. P., Dupuy, T. J., Endl, M., et al. 2018, AJ, 155, 159
Bowler, B. P., Liu, M. C., Shkolnik, E. L., & Tamura, M. 2015a, ApJS, 216, 7
Bowler, B. P., Shkolnik, E. L., Liu, M. C., et al. 2015b, ApJ, 806, 62
Brandt, T. D. 2018, ApJS, 239, 31
Brandt, T. D., Dupuy, T. J., & Bowler, B. P. 2019, AJ, 158, 140
Brandt, T. D., Dupuy, T. J., Bowler, B. P., et al. 2020, AJ, 160, 196
Brewer, J. M., Fischer, D. A., Valenti, J. A., & Piskunov, N. 2016, ApJS, 225, 32
Brewer, M.-M., & Carney, B. W. 2006, AJ, 131, 431
Burrows, A. 2013, RvMP, 85, 245
Burrows, A., Marley, M., Hubbard, W. B., et al. 1997, ApJ, 491, 856
Butler, R. P., Vogt, S. S., Laughlin, G., et al. 2017, AJ, 153, 208
Calissendorff, P., & Janson, M. 2018, A&A, 615, A149
Cheetham, A., Ségransan, D., Peretti, S., et al. 2018, A&A, 614, A16
Choi, J., Dotter, A., Conroy, C., et al. 2016, ApJ, 823, 102
Cochran, W. D., & Endl, M. 2008, PhST, 130, 014006
Cochran, W. D., Endl, M., McArthur, B., et al. 2004, ApJL, 611, L133
Cochran, W. D., & Hatzes, A. P. 1993, in ASP Conf. Ser. 36, Planets Around Pulsars, ed. J. A. Phillips, S. E. Thorsett, & S. R. Kulkarni (San Francisco: ASP), 267
Cochran, W. D., Hatzes, A. P., Butler, R. P., & Marcy, G. M. 1997, ApJ, 483, 457
Cochran, W. D., Tull, R. G., MacQueen, P. J., Paulson, D. B., & Endl, M. 2003, in ASP Conf. Ser. 294, Scientific Frontiers in Research on Extrasolar Planets, ed. D. Deming & S. Seager (San Francisco: ASP), 561
Crepp, J. R., Gonzales, E. J., Bechter, E. B., et al. 2016, ApJ, 831, 136
Crepp, J. R., Gonzales, E. J., Bowler, B. P., et al. 2018, ApJ, 864, 42
Crepp, J. R., Johnson, J. A., Howard, A. W., et al. 2013, ApJ, 774, 1
Crepp, J. R., Johnson, J. A., Howard, A. W., et al. 2014, ApJ, 781, 29

Cummings, J. D., Kalirai, J. S., Tremblay, P.-E., Ramirez-Ruiz, E., & Choi, J. 2018, ApJ, 866, 21
Cutri, R. M., Skrutskie, M. F., Van Dyk, S., et al. 2003, yCat, 2246, 0
De Mello, G. F. P., & da Silva, L. 1997, ApJL, 476, L89
Delgado Mena, E., Tsantaki, M., Adibekyan, V. Z., et al. 2017, A&A, 606, A94
Dotter, A. 2016, ApJS, 222, 8
Dupuy, T. J., Brandt, T. D., Kratter, K. M., & Bowler, B. P. 2019, ApJL, 871, L4
Dupuy, T. J., & Liu, M. C. 2012, ApJS, 201, 19
Dupuy, T. J., & Liu, M. C. 2017, ApJS, 231, 15
Eggleton, P. P. 1983, ApJ, 268, 368
Ekstrom, S., Georgy, C., Eggenberger, P., et al. 2012, A&A, 537, A146
Els, S. G., Sterzik, M. F., Marchis, F., et al. 2001, A&A, 370, L1
Endl, M., Brugamyer, E. J., Cochran, W. D., et al. 2016, ApJ, 818, 34
Endl, M., Kürster, M., & Els, S. 2000, A&A, 362, 585
Escorza, A., Karinkuzhi, D., Jorissen, A., et al. 2019, A&A, 626, A128
Farihi, J., Bond, H. E., Dufour, P., et al. 2013, MNRAS, 430, 652
Filippazzo, J. C., Rice, E. L., Faherty, J., et al. 2015, ApJ, 810, 158
Fischer, D. A., Marcy, G. W., & Spronck, J. F. P. 2014, ApJS, 210, 5
Foreman-Mackey, D., Hogg, D. W., Lang, D., & Goodman, J. 2013, PASP, 125, 306
Fuhrmann, K., Chini, R., Kaderhandt, L., Chen, Z., & Lachaume, R. 2017, MNRAS, 471, 3768
Gaia Collaboration, Brown, A. G. A., Vallenari, A., et al. 2018, A&A, 616, A1
Gianninas, A., Bergeron, P., & Ruiz, M. T. 2011, ApJ, 743, 138
Gray, R. O., Corbally, C. J., Garrison, R. F., et al. 2006, AJ, 132, 161
Gray, R. O., Corbally, C. J., Garrison, R. F., McFadden, M. T., & Robinson, P. E. 2003, AJ, 126, 2048
Hatzes, A. P., Cochran, W. D., Endl, M., et al. 2003, ApJ, 599, 1383
Hillenbrand, L. A., & White, R. J. 2004, ApJ, 604, 741
Hirsch, L. A., Ciardi, D. R., Howard, A. W., et al. 2019, ApJ, 878, 50
Howard, A. W., Johnson, J. A., Marcy, G. W., et al. 2010, ApJ, 721, 1467
Isaacson, H., & Fischer, D. 2010, ApJ, 725, 875
Kepler, S. O., Kleinman, S. J., Nitta, A., et al. 2007, MNRAS, 375, 1315
Konopacky, Q. M., Ghez, A. M., Barman, T. S., et al. 2010, ApJ, 711, 1087
Konopacky, Q. M., Marois, C., Macintosh, B. A., et al. 2016, AJ, 152, 28
Lafrenière, D., Marois, C., Doyon, R., Nadeau, D., & Artigau, É 2007, ApJ, 660, 770
Laughlin, G., Bodenheimer, P., & Adams, F. C. 1997, ApJ, 482, 420
Liebert, J., Bergeron, P., & Holberg, J. B. 2005, ApJS, 156, 47
Liu, M. C., Fischer, D. A., Graham, J. R., et al. 2002, ApJ, 571, 519
Luck, R. E. 2017, AJ, 153, 21
Maire, A. L., Molaverdikhani, K., Desidera, S., et al. 2020, A&A, 639, A47
Mann, A. W., Dupuy, T., Kraus, A. L., et al. 2019, ApJ, 871, 63
Marigo, P., & Girardi, L. 2007, A&A, 469, 239
Marois, C., Lafrenière, D., Doyon, R., Macintosh, B., & Nadeau, D. 2006, ApJ, 641, 556
Marois, C., Macintosh, B., & Véran, J.-P. 2010, Proc. SPIE, 7736, 77361J
Marsden, S. C., Petit, P., Jeffers, S. V., et al. 2014, MNRAS, 444, 3517
Mason, B. D., Hartkopf, W. I., & Miles, K. N. 2017, AJ, 154, 200
McClure, R. D., Fletcher, J. M., & Nemec, J. M. 1980, ApJL, 238, L35
Mints, A., & Hekker, S. 2017, A&A, 604, A108
Mugrauer, M., & Neuhäuser, R. 2005, MNRAS, 361, L15
Murgas, F., Jenkins, J. S., Rojo, P., A Jones, H. R., & Pinfield, D. J. 2013, A&A, 552, A27
Nakajima, T., Oppenheimer, B. R., Kulkarni, S. R., et al. 1995, Natur, 378, 463
Nelder, J. A., & Mead, R. 1965, CompJ, 7, 308
Parsons, S. G., Gänsicke, B. T., Marsh, T. R., et al. 2017, MNRAS, 470, 4473
Paxton, B., Bildsten, L., Dotter, A., et al. 2010, ApJS, 192, 3
Press, W., Teukolsky, S. A., Vetterling, W. T., & Flannery, B. P. 2007, Numerical Recipes: The Art of Scientific Computing (3rd ed.; Cambridge: Cambridge Univ. Press)
Queloz, D., Mayor, M., Weber, L., et al. 2000, A&A, 354, 99
Reddy, B. E., Lambert, D. L., & Allende Prieto, C. 2006, MNRAS, 367, 1329
Richmond, M. W., Droege, T. F., Gombert, G., et al. 2000, PASP, 112, 397
Rickman, E. L., Ségransan, D., Hagelberg, J., et al. 2020, A&A, 635, A203
Robertson, P., Endl, M., Cochran, W. D., et al. 2012, ApJ, 749, 39
Rodigas, T. J., Bergeron, P., Simon, A., et al. 2016, ApJ, 831, 177
Sahu, K. C., Anderson, J., Casertano, S., et al. 2017, Sci, 356, 1046
Saikia, S. B., Marvin, C. J., Jeffers, S. V., et al. 2018, A&A, 616, A108
Saladino, M. I., & Pols, O. R. 2019, A&A, 629, A103
Saumon, D., & Marley, M. S. 2008, ApJ, 689, 1327
Serenelli, A., Weiss, A., Aerts, C., et al. 2020, arXiv:2006.10868
Service, M., Lu, J. R., Campbell, R., et al. 2016, PASP, 128, 095004
Shetrone, M., Cornell, M. E., Fowler, J. R., et al. 2007, PASP, 119, 556
Simon, M., Guilloteau, S., Beck, T. L., et al. 2019, ApJ, 884, 42
Snellen, I. A. G., & Brown, A. G. A. 2018, NatAs, 2, 883
Soto, M. G., & Jenkins, J. S. 2018, A&A, 615, A76
Thalmann, C., Carson, J., Janson, M., et al. 2009, ApJL, 707, L123
Tinney, C. G., Butler, R. P., Marcy, G. W., et al. 2001, ApJ, 551, 507
Torres, G. 1999, PASP, 111, 169
Tsantaki, M., Sousa, S. G., Adibekyan, V. Z., et al. 2013, A&A, 555, A150
Tull, R. G. 1998, Proc. SPIE, 3355, 387
Tull, R. G., MacQueen, P. J., & Sneden, C. 1995, PASP, 107, 251
Wizinowich, P. 2013, PASP, 125, 798
Wizinowich, P., Acton, D. S., Shelton, C., et al. 2000, PASP, 112, 315
Yelda, S., Lu, J. R., Ghez, A. M., et al. 2010, ApJ, 725, 331
Zurlo, A., Vigan, A., Hagelberg, J., et al. 2013, A&A, 554, A21